



## Research

**Cite this article:** Hicks AL, Walker SW. 2024 Modelling and simulation of the cholesteric Landau-de Gennes model. *Proc. R. Soc. A* **480**: 20230813.

<https://doi.org/10.1098/rspa.2023.0813>

Received: 1 November 2023

Accepted: 5 April 2024

**Subject Areas:**

computational mathematics, mathematical modelling, applied mathematics

**Keywords:**

liquid crystals, Landau-de Gennes, finite-element method, cholesteric, gradient flow

**Author for correspondence:**

Shawn W. Walker

e-mail: [walker@math.lsu.edu](mailto:walker@math.lsu.edu)

# Modelling and simulation of the cholesteric Landau-de Gennes model

Andrew L. Hicks<sup>1</sup> and Shawn W. Walker<sup>2</sup>

<sup>1</sup>Department of Mathematics, and <sup>2</sup>Department of Mathematics, Center for Computation and Technology (CCT), Louisiana State University, Baton Rouge, LA 70803, USA

SWW, 0000-0002-8027-5789

This paper discusses modelling and numerical issues in the simulation of the Landau-de Gennes (LdG) model of nematic liquid crystals (LCs) with cholesteric effects. We propose a fully implicit, (weighted)  $L^2$  gradient flow for computing energy minimizers of the LdG model, and note a time-step restriction for the flow to be energy decreasing. Furthermore, we give a mesh size restriction, for finite-element discretizations, that is critical to avoid spurious numerical artifacts in discrete minimizers, particularly when simulating cholesteric LCs that exhibit ‘twist.’ Furthermore, we perform a computational exploration of the model and present several numerical simulations in three dimensions, on both slab geometries and spherical shells, with our finite-element method. The simulations are consistent with experiments, illustrate the richness of the cholesteric model, and demonstrate the importance of the mesh size restriction.

## 1. Introduction

New types of materials are a necessary component in many new technologies [1,2]. Liquid crystals (LCs), in particular, are finding innovative uses in many material design problems. Originally, nematic LCs were developed and commercialized for their optical properties [3–8], which is what enables LC displays.

Many nematic LCs are characterized by several material constants [9,10], which provide useful tuning parameters that can be tailored to specific applications. This paper is concerned with the modelling and

© 2024 The Authors. Published by the Royal Society under the terms of the Creative Commons Attribution License <http://creativecommons.org/licenses/by/4.0/>, which permits unrestricted use, provided the original author and source are credited.

numerical simulation of a particular sub-type of LC which are known as cholesteric nematic LCs, where the molecules have a chiral structure that affects their actuation and equilibrium behaviour [3,11,12]. Cholesteric LCs are present in many biological systems, such as viruses [13], chitin [14] and the structured colouring of the scarab beetle [15]. These materials often exhibit stripe patterns in their optical response, which can be exploited for engineering materials for the built environment [16,17]. This paper presents a numerical method and analysis for simulating cholesteric LCs in order to predict their structural features. Numerical modelling can yield greater insight into the functional effects of cholesteric LCs in biological systems and enable the design of programmable materials [18–20].

Many numerical methods and implementations exist for the standard Landau-de Gennes (LdG) model, e.g. [21–28]. These methods have also been extended to tackle cholesteric LCs [11,12,29,30]. However, to the best of our knowledge, a proper numerical analysis of the general LdG model that includes the cholesteric term appears to be lacking.

This paper gives an overview of numerical analysis issues that can arise in the general LdG model with cholesteric effects. We address both computing  $L^2$  gradient flow dynamics, as well as solving the equilibrium equations that characterize a local minimizer. In particular, time-step restrictions are needed to guarantee energy decrease of the gradient flow (e.g. even for the well-known convex-splitting scheme for handling the bulk potential). In addition, a mesh-size restriction appears that is not immediately obvious, i.e. if the computational mesh size is not small enough, unphysical solutions may occur (i.e. the computed local minimizer may exhibit numerical artifacts). Furthermore, we investigate two slightly different cholesteric models which can potentially produce different results depending on the material parameters (e.g. the twist) and whether other physics is coupled to the LC model (e.g. electric fields). We also demonstrate that the choice of initial condition can significantly affect which local minimizer is found, as well as the speed of convergence to a solution.

Part of the contribution of this paper is to present these issues, and how to handle them, to a diverse audience of computational scientists. Another contribution is to explore the cholesteric LdG model and illustrate the rich phenomena that result from it; see [11,12,17] for related work. Our presentation here should enable more robust computations for exploring the LC physics and device design of systems that are governed by the cholesteric LdG model.

We summarize some notational conventions we use in this paper. We focus on three dimensional LC models; thus 2-tensors are elements of  $\mathbb{R}^{3 \times 3}$  denoted by standard capital letters, e.g. the  $3 \times 3$  identity tensor is written as  $I$ . Constants and scalar-valued functions will be denoted by lowercase letters. Moreover, Greek letters will typically denote certain important functions and constants. Vectors will be denoted by boldface lowercase letters.

Let the  $D$  operator denote differentiation of a scalar-valued function with respect to each argument of a tensor; i.e. for any function  $\phi$  mapping to  $\mathbb{R}$ , define

$$D\phi(P) := \left[ \frac{\partial \phi}{\partial P_{ij}} \right]_{i,j=1}^3, \quad D^2\phi(P) := \left[ \frac{\partial^2 \phi}{\partial P_{ij} \partial P_{kl}} \right]_{i,j,k,l=1}^3, \quad \forall P \in \mathbb{R}^{3 \times 3},$$

i.e. the gradient and Hessian operators. For derivatives with respect to spatial coordinates, we use  $\partial_i \phi := \partial_{x_i} \phi$ , where  $\mathbf{x} = (x_1, x_2, x_3)^{\top}$  is the spatial coordinate, or we use the comma-subscript notation, e.g.  $\phi_{,i} := \partial_i \phi$  and  $P_{ij,k} := \partial_k P_{ij}$ .

Next, we define the  $L^2(\Omega)$ ,  $L^2(\Gamma)$  inner products and associated norms

$$(A, B)_{\Omega} := \int_{\Omega} A : B \, dx, \quad \|A\|_{0,\Omega}^2 := (A, A)_{\Omega}, \quad (A, B)_{\Gamma} := \int_{\Gamma} A : B \, dS(\mathbf{x}), \quad \|A\|_{0,\Gamma}^2 := (A, A)_{\Gamma},$$

where  $A, B$  are tensors and  $:$  is the Frobenius inner-product (similar relations hold for vectors and scalars). Moreover,  $|A| = \sqrt{A : A}$  is the Frobenius norm. We also have the  $H^1(\Omega)$  norm:  $\|P\|_{1,\Omega}^2 := \|P\|_{0,\Omega}^2 + \|\nabla P\|_{0,\Omega}^2$ .

## 2. Liquid crystal theory

We briefly review the LdG theory for a nematic LC phase.

### (a) Coarse-grained molecular theory

LCs are a *meso-phase* of matter where the ordered macroscopic state is between a spatially disordered liquid and a fully crystalline solid [31]. Nematic LC molecules are rod-like and are free to slide about, meaning no positional order is maintained. The (partial) spatial order that is maintained is *orientational*, i.e. the rod-like molecules prefer to be aligned with their neighbours due to molecular forces.

The  $Q$ -tensor order parameter, which represents the orientational order, can be derived via first principles (see [31]). Given a domain  $\Omega$  containing LC,  $Q$  is a tensor-valued function over  $\Omega$ , where  $Q(\mathbf{x})$  represents the (statistical) state of the LC (at  $\mathbf{x}$ ) and belongs to

$$\mathbf{S}_0 := \{Q \in \mathbb{R}^{3 \times 3} \mid Q^\dagger = Q, \text{tr}(Q) = 0\}. \quad (2.1)$$

Next, writing  $Q$  in its eigenframe, we have  $Q = \sum_{i=1}^3 \lambda_i \mathbf{e}_i \otimes \mathbf{e}_i$ , where  $\lambda_i \equiv \lambda_i(Q)$  are the eigenvalues of  $Q$ , and  $\mathbf{e}_i$  are the normalized eigenvectors. From the properties of  $Q$ , one can show that each  $\lambda_i$  satisfies  $-(1/3) \leq \lambda_i(Q) \leq (2/3)$  (for  $i = 1, 2, 3$ ). Also, since  $Q$  is traceless,  $\lambda_3 = -(\lambda_1 + \lambda_2)$ . If all eigenvalues are equal, they are 0 and we simply have  $Q = 0$ , which represents the isotropic state (no nematic order). Likewise, when all eigenvalues are different from one another, we have what is called the biaxial state. Most commonly, when only two of the eigenvalues are equal, we have the so-called *uniaxial* state, where  $Q$  may be expressed as

$$Q = s \left( \mathbf{n} \otimes \mathbf{n} - \frac{1}{3} I \right), \quad (2.2)$$

where  $s$  is called the *degree-of-orientation*, and is a measure of the orientational order of the LC molecules at each point, and  $\mathbf{n}$  is called the *director*, which has unit length,  $|\mathbf{n}| = 1$ , and represents the average direction in which the molecules are pointing. One can show that  $-\frac{1}{2} \leq s \leq 1$ . For many nematic LCs, the default state is usually uniaxial with a particular value of  $s$  that depends on the material. Typically, the optimal  $s$  is in the range  $0.5 \leq s \leq 0.8$  [3].

### (b) Landau-de Gennes theory

Next, we model the state of an LC system through a tensor-valued function  $Q: \Omega \rightarrow \mathbf{S}_0$ , where  $\Omega$  is the physical domain of interest that we assume throughout has Lipschitz boundary  $\Gamma$  with outward pointing unit normal vector  $\mathbf{v}$  (e.g. box-like domains and domains with smooth boundary are allowed). We assume that the equilibrium state of the LC is represented by a function  $Q$  that (locally) minimizes the LdG free energy [9,10,29]:

$$\mathcal{E}[Q] := \int_{\Omega} f(Q, \nabla Q) \, dx + \int_{\Omega} \psi(Q) \, dx + \int_{\Gamma} g(Q) \, dS(\mathbf{x}) + \int_{\Gamma} \phi(Q) \, dS(\mathbf{x}) - \int_{\Omega} \chi(Q) \, dx, \quad (2.3)$$

with the elastic energy (with twist component as in [11,29]) given by

$$f(Q, \nabla Q) := \frac{1}{2} (\ell_1 |\nabla Q|^2 + \ell_2 |\nabla \cdot Q|^2 + \ell_3 (\nabla Q)^\dagger \cdot \nabla Q + 4\ell_1 \tau_0 \nabla Q \cdot (\varepsilon \cdot Q)), \quad (2.4)$$

where  $\{\ell_i\}_{i=1}^3$  (units of  $\text{J m}^{-1}$ ) and  $\tau_0$  (units of  $\text{m}^{-1}$ ) are material dependent elastic constants, and we have the (frame indifferent) invariants  $|\nabla Q|^2 := Q_{ij,k} Q_{ij,k}$ ,  $|\nabla \cdot Q|^2 := Q_{ij,j} Q_{ik,k}$ ,  $(\nabla Q)^\dagger \cdot \nabla Q := Q_{ij,k} Q_{ik,j}$ ,  $\nabla Q \cdot (\varepsilon \cdot Q) := \varepsilon_{jkl} Q_{ik,l} Q_{ij}$ , where we use the convention of summation over repeated indices and  $\varepsilon_{jkl}$  is the Levi-Civita tensor. The transpose in the third term indicates to swap one of the  $Q$  indices with the derivative index. Note that taking  $\ell_i = 0$ , for  $i = 2, 3$  and  $\tau_0 = 0$  gives the often used one constant LdG model.

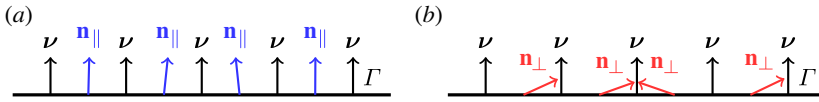


**Figure 1.** (a) Illustration of homeotropic anchoring. Here, the director  $\mathbf{n}$ , which we denote by  $\mathbf{n}_{\parallel}$ , is closely aligned with the outward normal vector  $\mathbf{v}$ ; the closeness of alignment is controlled by the constant  $w_0$ . (b) Illustration of planar degenerate anchoring. Here, the director  $\mathbf{n}$ , which we denote by  $\mathbf{n}_{\perp}$ , is closely aligned tangent to the surface; the closeness of alignment is controlled by the constants  $w_1$  and  $w_2$ .

Next, the bulk potential  $\psi$  is a double-well type of function that is given by

$$\psi(Q) = a_0 - \frac{a_2}{2} \text{tr}(Q^2) - \frac{a_3}{3} \text{tr}(Q^3) + \frac{a_4}{4} (\text{tr}(Q^2))^2. \quad (2.5)$$

Above,  $a_2, a_3, a_4$  are material parameters (units of  $\text{J m}^{-3}$ ) such that  $a_2, a_3, a_4$  are positive;  $a_0$  is a convenient constant to ensure  $\psi \geq 0$ . Stationary points of  $\psi$  are either uniaxial or isotropic  $Q$ -tensors [32]. Combined with (2.2), the critical values of the scalar order parameter  $s$  for  $\psi(Q(s))$ , where  $Q(s)$  is uniaxial, are  $s = 0$  (local maximum),  $s = (a_3 - \sqrt{a_3^2 + 24a_2a_4})/(4a_4)$  (local minimum) and the global minimum [33]:  $s_0 = (a_3 + \sqrt{a_3^2 + 24a_2a_4})/(4a_4)$ , and is typically in the range  $0.5 \leq s_0 \leq 0.8$  [3] for  $a_2$  sufficiently large positive, which we shall always assume. Note that, for thermotropic LCs,  $a_2$  is temperature dependent where  $a_2$  can become a large negative parameter for high enough temperature [10,31]. In this case,  $\psi$  becomes a convex function with a global minimum at  $Q = 0$  (the isotropic state). Though this potential is rather simplistic in that it does not guarantee that the eigenvalues of  $Q$  remain in the physical range (see earlier), it is effective in most modelling situations (cf. [32]).

The surface energy, composed of the quadratic  $g(Q)$  and higher-order  $\phi(Q)$ , accounts for *weak anchoring* of the LC (i.e. penalization of boundary conditions). For example, a Rapini–Papoular type anchoring energy [34] can be considered

$$g(Q) = \frac{w_0}{2} |Q - Q_{\Gamma}|^2 + \frac{w_1}{2} |\tilde{Q} - \tilde{Q}^{\perp}|^2 \quad \text{and} \quad \phi(Q) = \frac{w_2}{4} (|\tilde{Q}|^2 - s_0^2)^2, \quad (2.6)$$

where  $w_0, w_1$  and  $w_2$  are positive constants (units of  $\text{J m}^{-2}$ ),  $Q_{\Gamma}(\mathbf{x}) \in \mathbf{S}_0$  for all  $\mathbf{x} \in \Gamma$ , and  $s_0$  is the scalar order parameter of the uniaxial  $Q$  that minimizes the double well. Note that, typically,  $w_1 = w_2/2$  (see [35]), but we use two separate constants for the sake of generality. We set  $\tilde{Q} := Q + (s_0/3)I$ , and define the standard projection onto the plane orthogonal to  $\mathbf{v}$ , that is,  $Q^{\perp} := \Pi Q \Pi$  where  $\Pi = I - \mathbf{v} \otimes \mathbf{v}$ . We define  $Q_{\Gamma}$  to be uniaxial of the form  $Q_{\Gamma} = s_0(\mathbf{v} \otimes \mathbf{v} - I/3)$ . The  $w_0$  term in (2.6) models homeotropic (normal) anchoring, while  $w_1$  and  $w_2$  model planar degenerate anchoring. See figure 1 for an illustration.

The function  $\chi(\cdot)$  accounts for interactions with external fields. For example, the energy density of a dielectric LC with fixed boundary potential is given by  $-1/2 \mathbf{D} \cdot \mathbf{E}$  [36], where the electric displacement  $\mathbf{D}$  is related to the electric field  $\mathbf{E}$  by the linear constitutive law [3,37,38]:  $\mathbf{D} = \boldsymbol{\epsilon} \mathbf{E} = \bar{\boldsymbol{\epsilon}} \mathbf{E} + \boldsymbol{\epsilon}_a \mathbf{Q} \mathbf{E}$ ,  $\boldsymbol{\epsilon}(Q) = \bar{\boldsymbol{\epsilon}} I + \boldsymbol{\epsilon}_a Q$ , where  $\boldsymbol{\epsilon}$  is the LC material's dielectric tensor and  $\bar{\boldsymbol{\epsilon}}, \boldsymbol{\epsilon}_a$  are constitutive dielectric permittivities. Thus,  $-(1/2) \mathbf{D} \cdot \mathbf{E} = -(1/2) \bar{\boldsymbol{\epsilon}} |\mathbf{E}|^2 + \chi(Q)$ , where  $\chi(Q) = -(1/2) \boldsymbol{\epsilon}_a \mathbf{E} \cdot \mathbf{Q} \mathbf{E} \equiv -(1/2) \boldsymbol{\epsilon}_a \mathbf{E} \otimes \mathbf{E} : Q$ , with units  $\text{J m}^{-3}$ .

### (c) Non-dimensionalization

We start by noting that  $Q$  and  $s$  are already non-dimensional. Lengths and coordinates are non-dimensionalized by introducing a characteristic length  $\xi$ , e.g.  $\hat{\mathbf{x}} = \mathbf{x}/\xi$ , where  $\hat{\mathbf{x}}$  is non-dimensional. Then, set  $\ell_m$  to be the maximum or average of  $\{|\ell_i|\}_{i=1}^3$  and simply divide (2.3) by  $\ell_m \cdot \xi$  to obtain a dimensionless energy. This effectively rescales all spatial derivatives, integral measures and the various constants in the problem. Other non-dimensionalizations are possible (cf. [39, Sec. 2.]).

However,  $\psi(Q)$  and  $\phi(Q)$  are non-convex functions, which significantly affects the numerical analysis of the model. Thus, we describe their non-dimensionalization in more detail. Set

$c_0 := \psi(0) - \psi(Q(s_0))$  and define the non-dimensional bulk potential by  $\widehat{\psi}(Q) := \psi(Q)/c_0$ ; thus,  $\widehat{\psi}(0) - \widehat{\psi}(Q(s_0)) = 1$ . This immediately implies that  $|D\widehat{\psi}(Q)| = O(1)$ , as  $Q$  varies between the isotropic state and the global minimum of  $\widehat{\psi}$ . Then, upon introducing the non-dimensional parameter  $\eta := \sqrt{\ell_m/(c_0\xi^2)}$ , we have

$$\frac{1}{\ell_m\xi} \int_{\Omega} \psi(Q) \, d\mathbf{x} = \frac{1}{\eta^2} \int_{\widehat{\Omega}} \widehat{\psi}(Q) \, d\widehat{\mathbf{x}}, \quad (2.7)$$

where  $\widehat{\Omega}$  is the scaled domain. As for  $\phi(Q)$ , upon setting  $\widehat{\phi}(Q) = (|\widehat{Q}|^2 - s_0^2)^2/4$  and  $\omega := \ell_m/(w_2\xi)$ , we have

$$\frac{1}{\ell_m\xi} \int_{\Gamma} \phi(Q) \, dS(\mathbf{x}) = \frac{1}{\omega} \int_{\widehat{\Gamma}} \widehat{\phi}(Q) \, d\widehat{S}(\widehat{\mathbf{x}}), \quad (2.8)$$

where  $\widehat{\Gamma}$  is the scaled boundary. Then, the total non-dimensional energy is

$$\widehat{\mathcal{E}}[Q] = \int_{\widehat{\Omega}} \widehat{f}(Q, \widehat{\nabla}Q) \, d\widehat{\mathbf{x}} + \frac{1}{\eta^2} \int_{\widehat{\Omega}} \widehat{\psi}(Q) \, d\widehat{\mathbf{x}} + \int_{\widehat{\Gamma}} \widehat{g}(Q) \, d\widehat{S}(\widehat{\mathbf{x}}) + \frac{1}{\omega} \int_{\widehat{\Gamma}} \widehat{\phi}(Q) \, d\widehat{S}(\widehat{\mathbf{x}}) - \int_{\widehat{\Omega}} \widehat{\chi}(Q) \, d\widehat{\mathbf{x}}. \quad (2.9)$$

For simplicity, we drop the ‘hat’ notation for the remainder of the paper.

#### (d) The cholesteric LdG model

Cholesteric LCs are created by adding a chiral dopant (i.e. molecules with a chiral structure) to nematic LCs. This induces a helical superstructure on the nematic phase, which means the local behaviour of the LC is nematic (i.e. line segments are aligned with their immediate neighbours) but the larger, super-molecular arrangement of the line segments follows a helical structure with a certain periodicity (or pitch),  $p$ . The physical manifestation of the cholesteric phase is that the helix modulates the optical properties in a periodic fashion.

The cholesteric, LdG model in (2.3) can be obtained through a mapping procedure from the cholesteric, Oseen-Frank (director) LC model (see [9]). But we also consider a slightly different cholesteric model given in [11]. In the following sections, we relate this model (which we refer to as the cholesteric model) to the LdG model we have defined in §2b. The elastic energy in [11] is, mainly, a rewriting of the terms in (2.4). However, there is an implicit interference of the elastic energy in [11] with the bulk potential that brings up a modelling issue we highlight in part (ii) of this section.

#### (i) Elastic energy

The cholesteric model in [11] gives the elastic energy as

$$f_{\text{grad}}(Q) = \left(\frac{\check{\ell}_1}{2}\right) |\nabla \times Q + 2\tau_0 Q|^2 + \left(\frac{\check{\ell}_2}{2}\right) |\nabla \cdot Q|^2 + \left(\frac{\check{\ell}_{24}}{2}\right) (Q_{ij,k}Q_{ik,j} - Q_{ij,j}Q_{ik,k}), \quad (2.10)$$

where  $\check{\ell}_1, \check{\ell}_2, \check{\ell}_{24}$  are elastic constants,  $\tau_0 = 2\pi/p$  with  $p$  being the pitch, and  $\nabla \times Q = \varepsilon_{ikl}Q_{ij,k}\mathbf{e}^i \otimes \mathbf{e}^j$ , where  $\mathbf{e}^i$  is the  $i$ th vector in the standard basis of  $\mathbb{R}^3$ . This is referred to as the curl of  $Q$  and is consistent with the definition of curl for vectors, i.e. the columns of  $\nabla \times Q$  are the curls of the corresponding columns of  $Q$ . The term  $|\nabla \times Q + 2\tau_0 Q|^2$  is what frustrates the equilibrium state from having a constant director and models the chiral structure of the molecules. As we will see in the numerical results, choosing  $\tau_0 > 0$  causes a ‘twisting’ of the director throughout the LC domain.

It is a straightforward exercise in index notation to prove the identity  $|\nabla \times Q|^2 = Q_{ij,k}Q_{ij,k} - Q_{ij,k}Q_{ik,j}$ . Moreover, from the definition of  $\nabla \times Q$ , we have the identity  $(\nabla \times Q) : Q = (\varepsilon_{ikl}Q_{ij,k}\mathbf{e}^i \otimes \mathbf{e}^j) : Q = \varepsilon_{ikl}Q_{ij,k}Q_{ij}$ .

With this, we can rewrite (2.10) in the form of (2.4) by first noting that

$$\begin{aligned} \left(\frac{\check{\ell}_1}{2}\right) |\nabla \times Q + 2\tau_0 Q|^2 &= \left(\frac{\check{\ell}_1}{2}\right) Q_{ij,k} Q_{ij,k} - \left(\frac{\check{\ell}_1}{2}\right) Q_{ij,k} Q_{ik,j} \\ &\quad + \left(\frac{4\check{\ell}_1}{2}\right) \tau_0 \varepsilon_{ikl} Q_{ij,k} Q_{ij} + 2\check{\ell}_1 \tau_0^2 |Q|^2. \end{aligned}$$

From here, we note that  $\text{tr}(Q^2) \equiv |Q|^2$ , rearrange the terms and group them as

$$\begin{aligned} f_{\text{grad}}(Q) &= \left(\frac{\check{\ell}_1}{2}\right) Q_{ij,k} Q_{ij,k} + \left(\frac{\check{\ell}_2 - \check{\ell}_{24}}{2}\right) Q_{ij,j} Q_{ik,k} \\ &\quad + \left(\frac{\check{\ell}_{24} - \check{\ell}_1}{2}\right) Q_{ij,k} Q_{ik,j} + \left(\frac{4\check{\ell}_1}{2}\right) \tau_0 \varepsilon_{ikl} Q_{ij,k} Q_{ij} + 2\check{\ell}_1 \tau_0^2 \text{tr}(Q^2). \end{aligned} \quad (2.11)$$

We then use frame indifferent invariants to map these constants to the LdG elastic and twist energy densities as given in (2.4), i.e.  $\ell_1 = \check{\ell}_1$ ,  $\ell_2 = \check{\ell}_2 - \check{\ell}_{24}$ ,  $\ell_3 = \check{\ell}_{24} - \check{\ell}_1$ , where the twist constant  $\tau_0$  is the same in both models. Note that there is an extra term of  $|Q|^2 \equiv \text{tr}(Q^2)$  in (2.11) that is *not* found in (2.4) but does appear in (2.5). We discuss the implications of this in the next subsection.

## (ii) Alternative cholesteric model

In (2.4) and in [29], they consider the (cholesteric) elastic energy as not containing a  $\text{tr}(Q^2)$  term like [11] does. Indeed, keeping this term can have a significant effect on the behaviour of energy minimizers.

For simplicity of exposition, we assume all energies have been non-dimensionalized, take  $\ell_1 = 1$ ,  $\tau_0 > 0$ , and set the other elastic constants to zero. If we keep the  $\text{tr}(Q^2)$  term in (2.11), it will combine with the  $a_2$  coefficient in (2.5) to produce a new effective (non-dimensional) bulk potential in (2.9), namely

$$\tilde{\psi}(Q) = a_0 - \frac{a_2 - 4\ell_1 \eta^2 \tau_0^2}{2} \text{tr}(Q^2) - \frac{a_3}{3} \text{tr}(Q^3) + \frac{a_4}{4} (\text{tr}(Q^2))^2, \quad (2.12)$$

where  $\tilde{a}_2 = a_2 - 4\eta^2 \tau_0^2$  is the coefficient in front of  $\text{tr}(Q^2)$ . If  $\tau_0 = 15$  and  $a_2 = 1$ , for instance, then choosing  $\eta = 0.0408$  yields  $\tilde{a}_2 \approx 0.5$ , which is a significant change in the global minimum. One would have to choose  $\eta = 0.01$  to have  $\tilde{a}_2 > 0.9$ . Moreover, if  $\eta$  is not small enough to compensate for  $\tau_0$ , then  $\tilde{a}_2$  will be negative, which makes the  $\text{tr}(Q^2)$  term positive. If  $\tilde{a}_2$  is sufficiently large and negative, then  $\tilde{\psi}(Q)$  will be a convex function, with a single minimum at  $Q = 0$ , implying that the isotropic phase is preferred. Furthermore, in the case of thermotropic LCs, the  $\text{tr}(Q^2)$  coefficient depends on temperature. Thus, using (2.10) for the elastic energy leads to the effect that increasing the twist parameter is akin to increasing the temperature, which is not consistent with experiments. Figure 2 shows a comparison between the original double well and the modified one; clearly, the location of the global minima are different.

Hence, a moderate twist will change the effective double well (bulk) potential, which directly controls the nematic phase diagram of the LC; the severity of the change increases with the twist. To the best of our knowledge, the material doping discussed at the beginning of §2d, which is needed to create a cholesteric LC, should not change the nematic phase diagram. This seems to be an artifact of the model. Moreover, we note that choosing  $\eta$  sufficiently small to reduce the interference of the twist on the bulk potential is computationally inconvenient because it makes the problem more stiff; smaller time steps will be needed to ensure energy decrease in a gradient descent scheme. Therefore, we mainly adopt the approach in [29], which is justified in [9], and simply drop the  $\text{tr}(Q^2)$  term in (2.11). But we do provide a comparison with the model in [11] in §5f.

**Remark 2.1.** The surface anchoring energy proposed in [11] is the same as that given in (2.6) but with a trivial change in the constants.

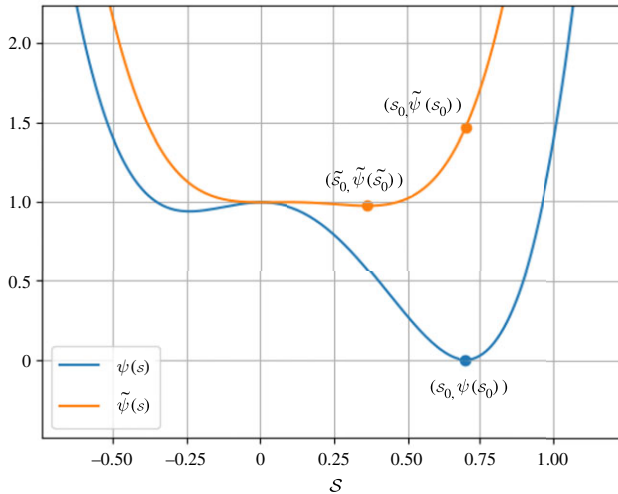


**Figure 2.** The two double wells from the two models. This compares the double well  $\psi$  in (2.5) to the effective double well  $\tilde{\psi}$  in (2.12), which arises when the alternate cholesteric model is used. Note that the global minima,  $s_0$  for  $\psi$  and  $\tilde{s}_0$  for  $\tilde{\psi}$ , of the two bulk potentials differ greatly.

### 3. Minimizing the Landau-de Gennes energy

Existence of a minimizer of (2.9) can be established through the direct method of the calculus of variations; for instance, see [23]. Computing a minimizer can, in principle, be done by solving the Euler–Lagrange equations associated with (2.9) (i.e. the first-order condition). However, these equations are nonlinear and the energy is non-convex, so simply applying Newton’s method will not necessarily converge nor produce a minimizer.

We begin by developing a weak formulation of the first order condition. Then, we describe multiple gradient flow schemes for finding (local) minimizers. The main purpose is to explain how different choices of the scheme (i.e. different implicit–explicit splittings) require different time-step restrictions that are affected by the bulk and boundary parameters  $\eta$  and  $\omega$ , and the twist parameter  $\tau_0$ .

#### (a) First-order condition

The minimization problem for the LdG energy functional (2.9), and associated first-order condition, is

$$\bar{Q} = \arg \min_{Q \in \mathbf{V}} \mathcal{E}[Q], \quad \delta_Q \mathcal{E}[\bar{Q}; P] = 0, \quad \forall P \in \mathbf{V}, \quad (3.1)$$

where  $\mathbf{V} := H^1(\Omega; \mathbf{S}_0)$  is the admissible space and  $\delta_Q \mathcal{E}[\cdot; \cdot]$  is the variational derivative of  $\mathcal{E}[\cdot]$ . Next, we introduce various bilinear forms that will be convenient in our analysis and for numerical computation. Let  $a_e(\cdot, \cdot) : \mathbf{V} \times \mathbf{V} \rightarrow \mathbb{R}$  be the bounded symmetric bilinear form defined by  $a_e(Q, P) := \ell_1(Q_{ij,k}, P_{ij,k})_\Omega + \ell_2(Q_{ij,j}, P_{ik,k})_\Omega + \ell_3(Q_{ij,k}, P_{ik,j})_\Omega$ . If  $\ell_1, \ell_2, \ell_3$  satisfy [23, Lem. 4.1]

$$0 < \ell_1, \quad -\ell_1 < \ell_3 < 2\ell_1, \quad -\frac{3}{5}\ell_1 - \frac{1}{10}\ell_3 < \ell_2, \quad (3.2)$$

then there is a constant  $c > 0$  such that  $a_e(P, P) \geq c \|\nabla P\|_{0,\Omega}^2$ , for all  $P \in \mathbf{V}$ .

Next, let  $a_s(\cdot, \cdot) : \mathbf{V} \times \mathbf{V} \rightarrow \mathbb{R}$  be the bounded symmetric bilinear form defined by  $a_s(Q, P) := w_0(Q, P)_\Gamma + w_1(Q - Q^\perp, P)_\Gamma$ , where  $w_0, w_1 \geq 0$ . If either  $w_0$  or  $w_1$  is positive, then there exists a constant  $\alpha_1 > 0$  such that

$$a_e(P, P) + a_s(P, P) \geq \alpha_1 \|P\|_{1,\Omega}^2, \quad \forall P \in \mathbf{V}. \quad (3.3)$$

See [40] for a proof of (3.3). We also have the bilinear form  $a_t(\cdot, \cdot): \mathbf{V} \times \mathbf{V} \rightarrow \mathbb{R}$ , which is *not* coercive, accounting for the twist term  $a_t(Q, P) := 2\ell_1\tau_0[\varepsilon_{ikl}(Q_{jk,l}, P_{ij})_\Omega + \varepsilon_{ikl}(P_{jk,l}, Q_{ij})_\Omega]$ . For later use, we define one bilinear form to contain the previously defined forms

$$a(Q, P) := a_e(Q, P) + a_t(Q, P) + a_s(Q, P), \quad (3.4)$$

and note that there is a constant  $c_0 > 0$  such that  $|a(Q, P)| \leq c_0\|Q\|_{1,\Omega}\|P\|_{1,\Omega}$ . We also introduce the linear form  $l_{\text{rhs}}(\cdot): \mathbf{V} \rightarrow \mathbb{R}$ :

$$l_{\text{rhs}}(P) := (\chi(P), 1)_\Omega + w_0(Q_\Gamma, P)_\Gamma + w_1\left(-\frac{s_0}{3}\mathbf{v} \otimes \mathbf{v}, P\right)_\Gamma. \quad (3.5)$$

We can now write  $\mathcal{E}[Q]$  in the form

$$\mathcal{E}[Q] = \left(\frac{1}{2}\right)a(Q, Q) + \left(\frac{1}{\eta^2}\right)(\psi(Q), 1)_\Omega + \left(\frac{1}{\omega}\right)(\phi(Q), 1)_\Gamma - l_{\text{rhs}}(Q), \quad (3.6)$$

which yields the following expression for the first variation of  $\mathcal{E}$ :

$$\delta_Q\mathcal{E}[Q; P] = a(Q, P) + \left(\frac{1}{\eta^2}\right)(D\psi(Q), P)_\Omega + \left(\frac{1}{\omega}\right)(D\phi(Q), P)_\Gamma - l_{\text{rhs}}(P). \quad (3.7)$$

Combining with (3.1), we find that  $\bar{Q}$  satisfies a tensor-valued, anisotropic, elliptic partial differential equation (PDE) *system* defined over  $\Omega$  with a tensor-valued Robin boundary condition. For instance, in terms of indices  $1 \leq i, j \leq 3$ , the bulk PDE (with  $\chi$  taken from the dielectric LC energy density as in §2b) is

$$\begin{aligned} & -\ell_1 Q_{ij,kk} - \ell_2 Q_{ik,kj} - \ell_3 Q_{ik,jk} - 4\ell_1\tau_0\varepsilon_{ilk}Q_{lj,k} \\ & + \frac{1}{\eta^2}(-a_2 Q_{ij} - a_3(Q^2)_{ij} + a_4|Q|^2 Q_{ij}) = -\frac{1}{2}\varepsilon_a(\mathbf{E} \otimes \mathbf{E})_{ij}, \quad \text{in } \Omega, \end{aligned} \quad (3.8)$$

where only the traceless part of the tensor equation is considered. In (3.8), note that the term  $4\ell_1\tau_0\varepsilon_{ilk}Q_{lj,k}$  is analogous to a convective term, e.g.  $(V \cdot \nabla)Q$ , where  $V_{ilk} = 4\ell_1\tau_0\varepsilon_{ilk}$  is like a ‘velocity’. It is well known [41] that convection-diffusion problems present some difficulties in their numerical approximation, especially when the velocity is large. This is the case here when  $\tau_0$  is large, which manifests as a mesh-size restriction in theorem 4.2, as well as restricting the time-step when a popular convex-splitting scheme is used for finding an energy minimum (see theorem 3.2).

## (b) Gradient flow

We look for an energy minimizer using a gradient flow strategy [22,26,27,29] applied to the energy (2.9). Let  $t$  represent ‘time’ and suppose that  $Q \equiv Q(x, t)$  evolves by an  $L^2(\Omega)$  gradient flow

$$(\partial_t Q(\cdot, t), P)_\Omega = -\delta_Q\mathcal{E}[Q; P], \quad \forall P \in \mathbf{V}, \quad (3.9)$$

where  $Q(x, 0) = Q_0 \in \mathbf{V}$  is the initial guess for the flow. Formally, the solution of (3.9) will converge to a local minimizer. In this case,  $Q(x, t)$  satisfies a parabolic PDE (in strong form), and by the standard theory of parabolic PDEs, it has a unique solution. Gradient flows are related to the natural relaxation that many physical systems undergo, including LCs, which is why we use it in our simulations. Directly minimizing  $\mathcal{E}$  by some other optimization technique is also possible and may yield other minimizers that are not commonly observed in experiment.

We discretize (3.9) in time by first letting  $Q_k(x) \approx Q(x, k\delta t)$ , where  $\delta t > 0$  is a finite time step and  $k$  is the time index. Next, we replace  $\partial_t Q(\cdot, t)$  by a finite difference approximation, so then (3.9)

becomes a sequence of elliptic problems. In other words, given  $Q_k$ , find  $Q_{k+1} \in \mathbf{V}$  such that

$$\delta t^{-1}(Q_{k+1} - Q_k, P)_{\delta t} = -\delta_Q \mathcal{E}[Q_{k+1}; P], \quad \forall P \in \mathbf{V}, \quad (3.10)$$

where we have defined a time-stepping inner product  $(\cdot, \cdot)_{\delta t}$  by

$$(P, T)_{\delta t} := \frac{1}{\eta^2}(P, T)_{\Omega} + \frac{1}{\omega}(P, T)_{\Gamma}. \quad (3.11)$$

We also define a norm by  $\|P\|_{\delta t}^2 := (P, P)_{\delta t}$ . One can show that (3.10) is equivalent to a minimizing movements strategy [42]

$$Q_{k+1} = \arg \min_{Q \in \mathbf{V}} \mathcal{F}^k(Q), \quad \mathcal{F}^k(Q) := \frac{1}{2\delta t} \|Q - Q_k\|_{\delta t}^2 + \mathcal{E}[Q], \quad (3.12)$$

which immediately yields the useful property  $\mathcal{F}^k(Q_{k+1}) \leq \mathcal{F}^k(Q_k) \leq \mathcal{F}^{k-1}(Q_k)$  and implies that  $\mathcal{E}[Q_{k+1}] \leq \mathcal{E}[Q_k]$  for all  $k$ . In practice, we iterate until we reach a final iteration index or some other stopping criteria (see §5a). However, (3.10) is a *fully implicit* equation and requires an iterative solution because of the nonlinearities in  $\psi(Q)$  and  $\phi(Q)$ . The following theorem, whose proof can be found in appendix A(a) and also [40], gives a time-step restriction to ensure energy decrease.

**Theorem 3.1.** *The sequence  $\{Q_k\}_{k=0}^{\infty}$  defined by the method in (3.10) is monotonically energy decreasing, i.e.  $\mathcal{E}[Q_{k+1}] \leq \mathcal{E}[Q_k]$ , provided that  $\delta t \leq 2/\max\{a_2 + a_3^2/a_4, 2s_0^2/3\}$ .*

The time step restriction in theorem 3.1 involves non-dimensional constants of  $O(1)$ . However, the time-step inner product (3.11) used in (3.10) accounts for the strength of the non-convex terms through the positive constants  $\eta$  and  $\omega$ . In other words, when either  $\eta$  and  $\omega$  are small, the minimizing movements scheme in (3.12) penalizes  $Q_{k+1} - Q_k$  to be small. Hence, the minimization sequence will take more iterations when either  $\eta$  and  $\omega$  are small.

Other types of time-discretizations can be used, such as implicit–explicit methods. But they usually have more stringent time-step restrictions. Another related strategy is *convex-splitting* which is popular in gradient flow schemes [27,43,44]. For instance, let  $\psi(Q) = \psi_c(Q) - \psi_e(Q)$ , where  $\psi_c$  and  $\psi_e$  are convex functions of  $Q$ . We modify (3.10) by treating  $\psi_c$  implicitly and  $\psi_e$  explicitly. For simplicity, we drop the nonlinear  $\phi$  term, and simplify the time stepping inner product to  $(P, T)_{\delta t} = (P, T)_{\Omega}$ . Then, (3.10) is replaced by the following. Given  $Q_k$ , find  $Q_{k+1} \in \mathbf{V}$  such that

$$\begin{aligned} \delta t^{-1}(Q_{k+1} - Q_k, P)_{\Omega} + a(Q_{k+1}, P) + \left(\frac{1}{\eta^2}\right) (D\psi_c(Q_{k+1}), P)_{\Omega} \\ = I_{\text{rhs}}(P) + \left(\frac{1}{\eta^2}\right) (D\psi_e(Q_k), P)_{\Omega}, \quad \forall P \in \mathbf{V}. \end{aligned} \quad (3.13)$$

This scheme also has an energy decrease property with a time-step restriction.

**Theorem 3.2.** *The sequence  $\{Q_k\}_{k=0}^{\infty}$  defined by the method in (3.13) is monotonically energy decreasing, i.e.  $\mathcal{E}[Q_{k+1}] \leq \mathcal{E}[Q_k]$ , provided that  $\delta t \leq 2\alpha_1/(108\ell_1^2\tau_0^2 - \alpha_1^2)$ , where  $\alpha_1$  is the coercivity constant in (3.3). If  $|\tau_0| \leq \alpha_1/(2\sqrt{27}\ell_1)$ , there is no restriction on  $\delta t$ .*

A proof of this result may be found in [40]. Usually, a convex splitting scheme is used to *avoid* a time-step restriction. However, the above discussion shows that a sufficiently large  $\tau_0$  will cause a restriction. Moreover, according to [44], a convex splitting scheme is nothing but a fully implicit scheme with time re-scaled (when  $\tau_0 = 0$ ). Thus, we always use the fully implicit scheme as our gradient descent strategy to find a minimizer of (3.1).

## 4. Finite-element method

We approximate (3.10) by a finite-element method [45]. In doing so, we assume that  $\Omega \subset \mathbb{R}^3$  is discretized by a conforming shape regular triangulation  $\mathcal{T}_h = \{T_i\}$  consisting of tetrahedra. Theorem 4.2 presents an error estimate for our finite-element discretization of the equilibrium problem (i.e. first-order condition in (3.1)).

## (a) Spatial Discretization

Let  $\mathbb{M}_h(\Omega_h)$  be the space of continuous, piecewise Lagrange polynomial functions on  $\Omega_h$ , subordinate to the mesh  $\mathcal{T}_h$  of  $\Omega_h$ , with polynomial degree  $r \geq 1$ . We discretize (3.10) by approximating  $Q$  by a finite-element function  $Q_h$ . Note that  $\mathbf{S}_0$  can be uniquely identified with a five dimensional vector space [21], i.e. there exists  $3 \times 3$ , symmetric traceless basis matrices  $\{E^i\}_{i=1}^5$  such that any  $Q \in \mathbf{S}_0$  can be uniquely expressed as  $Q = q_i E^i$ , for some coefficient functions  $q_1, \dots, q_5$ . With this, we define the tensor finite-element space

$$\mathbb{S}_h(\Omega_h) := \{P \in C^0(\Omega_h; \mathbf{S}_0) \mid P = q_{i,h} E^i, q_{i,h} \in \mathbb{M}_h(\Omega_h), 1 \leq i \leq 5\}, \quad (4.1)$$

and let  $Q_h \in \mathbf{V}_h := \mathbb{S}_h(\Omega_h) \subset \mathbf{V}$ . Thus,  $Q_h = q_{i,h} E^i$ , and  $q_{i,h} \in H^1(\Omega)$  for  $i = 1, \dots, 5$ .

The fully discrete  $L^2$ -gradient flow now follows from (3.10), i.e. given  $Q_{h,k}$ , find  $Q_{h,k+1} \in \mathbf{V}_h$  such that

$$\delta t^{-1}(Q_{h,k+1} - Q_{h,k}, P_h)_{\delta t} = -\delta_Q \mathcal{E}[Q_{h,k+1}; P_h], \quad \forall P_h \in \mathbf{V}_h. \quad (4.2)$$

We iterate this procedure until some stopping criteria is achieved (see §5a). Since  $\mathbf{V}_h \subset \mathbf{V}$ , the same arguments in §3b still hold when replacing  $\mathbf{V}$  by  $\mathbf{V}_h$ . Therefore, the same time-stepping restrictions apply to the fully discrete formulation.

## (b) Error estimate for the equilibrium problem

We present an error estimate for finite-element approximations of a local minimizer of the LdG energy  $\mathcal{E}[\cdot]$ . If  $Q \in \mathbf{V}$  is a local minimizer of  $\mathcal{E}[\cdot]$ , then it satisfies the first-order condition in (3.1). Moreover, if  $Q_h \in \mathbf{V}_h$  is a local minimizer of  $\mathcal{E}[\cdot]$  (over the discrete space  $\mathbf{V}_h$ ), then

$$\begin{aligned} \delta \mathcal{E}[Q_h](P_h) &= a(Q_h, P_h) + \left(\frac{1}{\eta^2}\right) (D\psi(Q_h), P_h)_\Omega \\ &\quad + \left(\frac{1}{\omega}\right) (D\phi(Q_h), P_h)_\Gamma - l_{\text{rhs}}(P_h) = 0, \quad \forall P_h \in \mathbf{V}_h. \end{aligned} \quad (4.3)$$

The error estimate in theorem 4.2 is built on the following assumption, which says that the energy landscape around a minimizer is not too flat.

**Assumption 4.1 (Isolated minimizer and coercivity).** For a given local minimizer  $Q$  of  $\mathcal{E}$ , we assume there exists  $\zeta > 0$  such that for all  $\tilde{Q}$  with  $\|Q - \tilde{Q}\|_{1,\Omega} < \zeta$ , we have  $\mathcal{E}[Q] \leq \mathcal{E}[\tilde{Q}]$ , and for some  $m_0 > 0$ ,

$$\begin{aligned} \delta^2 \mathcal{E}[\tilde{Q}](P, P) &= a(P, P) + \left(\frac{1}{\eta^2}\right) (P, D^2\psi(\tilde{Q})P)_\Omega \\ &\quad + \left(\frac{1}{\omega}\right) (P, D^2\phi(\tilde{Q})P)_\Gamma \geq m_0 \|P\|_{1,\Omega}^2, \quad \forall P \in \mathbf{V}. \end{aligned} \quad (4.4)$$

In order to avoid additional technicalities, we assume that if  $Q$  is a solution of (3.1), then it has the additional regularity  $Q \in H^2(\Omega)$ . Moreover, we also assume an associated adjoint problem also enjoys additional  $H^2(\Omega)$  regularity; see remark A.4 (in the appendix) for further details. We have the following result that yields an error estimate for the finite-element solution  $Q_h$ , which requires a *restriction* on the mesh size  $h$ .

**Theorem 4.2.** *Let  $Q \in \mathbf{V}$  be a local minimizer of  $\mathcal{E}[\cdot]$  that satisfies (3.1) and also satisfies  $Q \in H^2(\Omega)$ , and let  $Q_h \in \mathbf{V}_h$  be a local minimizer of  $\mathcal{E}[\cdot]$  that satisfies (4.3). Moreover, adopt assumption 4.1 and assume that  $\|Q - Q_h\|_{1,\Omega} < \zeta$ . Then, there exists  $c > 0$  such that for all  $h \leq h_0$ , we have  $\|Q - Q_h\|_{1,\Omega} \leq ch \|Q\|_{2,\Omega}$ ,*

where

$$h_0 = \left( \frac{\alpha_1}{k + (a'/\eta^2) + (s''/\omega^2)} \right)^{1/2} \frac{1}{\sqrt{8}(c_0 + \beta'_1/\eta^2 + \beta'_2/\omega)c_2c_3}, \quad (4.5)$$

where  $k = \max((216\ell_1^2\tau_0^2/\alpha_1) - (\alpha_1/2), 0)$ ,  $c_1, c_2, c_3, \beta'_1, \beta'_2, a'$  and  $s''$  are constants depending on the domain, and

$$c_0 = \ell_1 + 3\ell_2 + \ell_3 + 4\ell_1\sqrt{27}\tau_0 + \beta_3(w_0 + 3w_1) \quad (4.6)$$

is the constant such that  $|a(Q, P)| \leq c_0\|Q\|_{1,\Omega}\|P\|_{1,\Omega}$ , with  $\beta_3$  also depending on the domain.

The proof of theorem 4.2 is found in §Ab, as well as [40]. Note that (4.5) says that small values of  $\eta$  and  $\omega$ , and large values of  $\tau_0$ , lead to small values of  $h_0$ . Furthermore, theorem 4.2 says there is *no* error estimate if the mesh size is too large. This means that the discrete problem may have *no* connection to the physical problem of interest.

## 5. Simulations

We present several simulations that illustrate the cholesteric LdG model on both a slab geometry and a spherical shell for a range of twist parameters. We illustrate both the richness of the model, as well as issues that can arise when the mesh size is not small enough. Our software is implemented in Firedrake [46], which heavily uses the PETSc library [47]. We used Paraview to visualize our simulations. We simulated on two of the machines owned by the LSU Department of Mathematics. Each machine was equipped with two Intel Xeon Gold 6242R processors running at 3.10/4.10 GHz, as well as a 768 GiB RAM. We ran our simulations on a single node using 25 processes.

### (a) Minimization technique

As discussed in §3b, the gradient descent method can be used to find a local minimizer of the LdG equilibrium problem. In our implementation, we apply this method to the finite-element discretization of the problem. At each time step, we must solve a nonlinear system in (4.2), so Firedrake's built-in nonlinear solver (which utilizes Newton's method) is employed. We use the Geometric agglomerated Algebraic MultiGrid (GAMG) preconditioner, as well as the Minimal Residual Method (MINRES) for our Krylov subspace method.

However, the fully implicit gradient descent method we use comes with a time-step restriction (see theorem 3.1) that is affected by  $\eta$  and  $\omega$  through the minimizing movements inner product (3.12), as well as the twist  $\tau_0$ . This can lead to excessive computation times. Therefore, in practice, we start with a time step that satisfies the various restrictions given earlier and compute several steps (e.g. we start with a time step of  $\delta t = 0.001$  and we compute 50 steps). Then, we increase the time step by a factor of 10 and do several more steps (e.g. 50), checking that the energy continues to decrease with each step. If the energy does not decrease after increasing the time step, or if the solver diverges, then we go back to the smaller time step and perform more iterations before attempting to increase the time step again. In practice, however, the energy always decreased in our simulations; the only situation in which we had to go back to the smaller time step was when the solver diverged. This continues until  $\delta t$  reaches a maximum value of  $\delta t = 100\,000$ , after which we continue iterating. During this procedure, for any value of  $\delta t$ , if the energy decrease between successive iterates is less than a tolerance (e.g.  $10^{-6}$ ), then we stop iterating and solve the equilibrium problem directly (i.e. no gradient descent). If the nonlinear solver for the equilibrium problem diverges, then we continue with several more gradient descent iterations. Despite the *ad hoc* nature of this procedure, it was effective in obtaining (discrete) local minimizers of the discrete LdG energy in a reasonable amount of time.

## (b) Parameter choices and visualization

The following parameter values were used for all simulations in §5c, d and e. The coefficients of the double well in (2.5) were chosen as

$$a_0 = 1, \quad a_2 = 7.502104, \quad a_3 = 60.975813 \quad \text{and} \quad a_4 = 66.519069. \quad (5.1)$$

The function  $\psi(Q)$  has a global minimum at  $Q_* = s_0(\mathbf{l} \otimes \mathbf{l} - I/3)$ , where  $\mathbf{l} \in \mathbb{R}^3$  is any unit vector, and  $s_0 = 0.7$ . The other coefficients are given by  $\ell_1 = 1.0$ ,  $\ell_2 = \ell_3 = 0$ , and  $\eta = 0.1$ . We conducted experiments with both homeotropic anchoring (i.e.  $w_0 = 10.0$ ,  $w_1 = w_2 = 0$ ) and planar degenerate anchoring (i.e.  $w_0 = 0$ ,  $w_1 = w_2 = 10.0$  and  $\omega = 0.1$ ). The twist was varied, with values typically chosen as  $\tau_0 = 0, 5, 10, 15, 20, 25$ . In §5f, a different set of parameters was used corresponding to the LC 5CB.

The numerical solution for  $Q$  is visualized by first performing an eigendecomposition of  $Q$  at each node of the mesh. We then set  $\mathbf{n}$  to be the eigenvector of  $Q$  corresponding to the largest eigenvalue of  $Q$ . If  $Q$  has a uniaxial form, then this choice of  $\mathbf{n}$  is consistent with (2.2). Finally, we compute  $|\mathbf{n} \cdot \mathbf{r}|$ , where  $\mathbf{r}$  is a given vector that corresponds to the computational domain, and visualize  $|\mathbf{n} \cdot \mathbf{r}|$  as a scalar field. Typically,  $\mathbf{r}$  is chosen to face a hypothetical viewer, and this varies depending on the geometry of the LC domain. Thus,  $|\mathbf{n} \cdot \mathbf{r}| = 0$  means the LCs are facing orthogonal to the viewer's line of sight, and  $|\mathbf{n} \cdot \mathbf{r}| = 1$  means the LCs are facing the viewer directly.

## (c) Slab configuration

### (i) Experimental set-up

The domain  $\Omega$  is a rectangular solid (slab geometry), where  $\Omega = (0, 2) \times (0, 2) \times (0, 0.2)$ . The boundary is partitioned as  $\Gamma = \Gamma_1 \cup \Gamma_0$  where  $\Gamma_1 = (0, 2) \times (0, 2) \times \{0, 0.2\}$  (top and bottom of the slab) and  $\Gamma_0 = \Gamma \setminus \Gamma_1$  (sides of the slab). Then, in the formulation (3.10), we replace  $\Gamma$  with  $\Gamma_1$ , i.e. we enforce the weak anchoring condition on  $\Gamma_1$  and use a zero Neumann condition on  $\Gamma_0$ . For the finite-element discretized domain  $\Omega_h$ , we chose a mesh size of  $h = 0.02$ .

The initial condition was chosen as follows. First, define

$$\mathbf{w}_1 = (0, \cos(\tau_0 x_1), \sin(\tau_0 x_1))^{\dagger}, \quad \mathbf{w}_2 = (\cos(\tau_0 x_2), \sin(\tau_0 x_2), 0)^{\dagger}. \quad (5.2)$$

Then for  $i = 1, 2$ , we define  $\mathbf{n}_i = \mathbf{w}_i / |\mathbf{w}_i|$ , and  $Q_i := s_0(\mathbf{n}_i \otimes \mathbf{n}_i - I/3)$ . Each  $Q_i$  corresponds to a helical configuration of the director field, with period given by  $2\pi/\tau_0$ . Then, choosing  $\rho = (\cos(\tau_0 x_1) \cos(\tau_0 x_2) + 1)/2$ , we set

$$Q_0 = (1 - \rho)Q_1 + \rho Q_2. \quad (5.3)$$

See figure 3 for a visualization of the initial condition  $Q_0$  and the computed local minimizers for both homeotropic and planar degenerate anchoring for a range of twist values  $\tau_0$ . Note that the colour corresponds to  $|\mathbf{n} \cdot \mathbf{r}|$  with  $\mathbf{r} = \mathbf{e}_3$  (see §5b).

### (ii) Results

Table 1 lists the (non-dimensional) energies of the initial condition for each  $\tau_0$  compared to the energies of the equilibrium state (a local minimizer), for both homeotropic and planar degenerate anchoring. Figure 3 (middle column) depicts the final equilibrium solutions with homeotropic anchoring, all of which had very regular stripe patterns, except when  $\tau_0 = 5$  where the solution for the homeotropic case consisted of the director pointing normal to the surface on the entire domain. In addition, as  $\tau_0$  increased, the final stripe patterns aligned more with the diagonal of the slab. This is most likely due to the zero Neumann condition imposed on the sides. If a periodic boundary condition were used, then the final configuration would be invariant to rotations of the  $\mathbf{e}_1, \mathbf{e}_2$  plane. We were not able to enforce this condition because of a limitation of Firedrake.

For the planar degenerate anchoring case (figure 3, right column), similar striped patterns occurred in the equilibrium solutions for each twist value. However, the alignment with the diagonal was not quite as pronounced. Moreover, the transition between stripes was

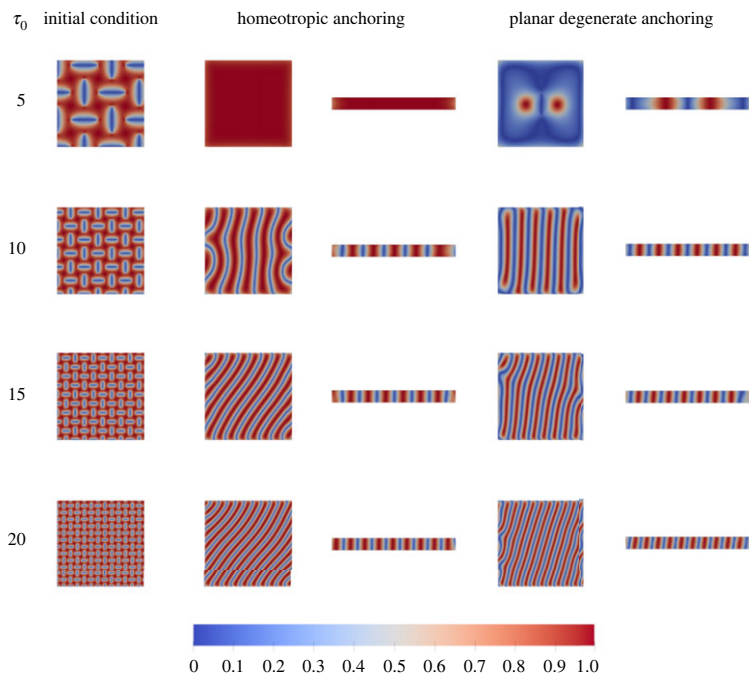


**Figure 3.** Slab geometry:  $2 \times 2 \times 0.2$  (S5c, part (ii)). Colour is proportional to  $|\mathbf{n} \cdot \mathbf{e}_3|$ . Initial condition column shows top view (viewing the  $xy$  plane) of slab. Homeotropic anchoring columns show the top view and a vertical slice (viewing the  $xz$  plane) through the middle of the slab. Planar degenerate anchoring columns have the same format.

**Table 1.** Energies for the slab ( $2 \times 2 \times 0.2$ ) in figure 3.

$\tau_0$	homeotropic anchoring		planar degenerate anchoring	
	initial energy	final energy	initial energy	final energy
0	39.20061947	32.86058337	0.0	0.0
5	49.25887441	-2.64966269	43.13556899	-11.06811563
10	70.41495358	-41.83731193	65.18722048	-51.78216459
15	104.88188461	-122.7420167	100.38078589	-133.893747
20	151.32789951	-254.83515683	147.15907691	-265.87890179

slightly different from the homeotropic case and the period was different. For instance,  $\tau_0 = 20$  corresponds to an ideal period of  $p = 2\pi/\tau_0 \approx 0.314$ , but the measured period from the simulation was  $p = 0.35$  ( $p = 0.38$ ) for the homeotropic (planar degenerate) case. We also note that in the planar degenerate case, with  $\tau_0 = 5$ , the director is mainly tangential, except for two small, disconnected regions where the director becomes parallel to  $\mathbf{e}_3$ . This is because the anchoring constants, which are set to  $w_1 = w_2 = (1/\omega) = 10$ , outweigh the twist. Simulation times varied, ranging from 0 to 41 h for the homeotropic case, and 0 to 16 h for the planar degenerate case. Times were generally shorter for the planar degenerate case.

## (d) Shell configuration

### (i) Details

The domain  $\Omega$  is a spherical annulus (shell), where two choices were used. For the first shell, we set  $\Omega = \Omega_{\text{shell},0} := \mathcal{B}(\mathbf{0}, 1) \setminus \overline{\mathcal{B}}(\mathbf{0}, 0.9)$ , where  $\mathcal{B}(\mathbf{0}, r)$  is an open ball of radius  $r$ . For the finite-element discretization  $\Omega_h$ , we set the mesh size to be  $h = 0.02$ . For the initial condition, when  $\tau_0 > 0$ , we let

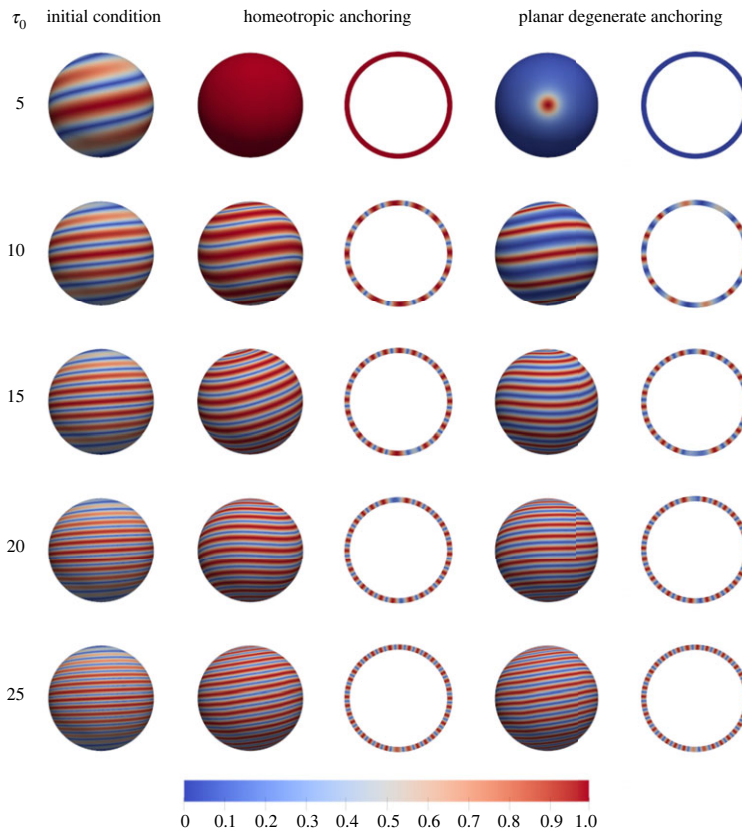


**Figure 4.** Centred shell ( $\Omega_{\text{shell},0}$ ), front view (viewing the  $yz$  plane) (§5d, part (ii)). Colour is proportional to  $|\mathbf{n} \cdot \mathbf{r}|$  with  $\mathbf{r} = \mathbf{x}/|\mathbf{x}|$ . Homeotropic anchoring columns show the outer boundary and a vertical slice through the shell. Planar degenerate anchoring columns have the same format.

$\mathbf{w} = \mathbf{w}(x_1, x_2, x_3) = (\cos(\tau_0 x_3), \sin(\tau_0 x_3), 0)^\dagger$ . Then, similarly to the initial conditions for the slabs, we set  $\mathbf{n} = \mathbf{w}/|\mathbf{w}|$  and

$$Q_0 = s_0 \left( \mathbf{n} \otimes \mathbf{n} - \frac{I}{3} \right). \tag{5.4}$$

For  $\tau_0 = 0$ , we let  $\mathbf{n} = \mathbf{x}/|\mathbf{x}|$ , and set  $Q_0$  as in (5.4).

The far left column of figures 4 and 5 depicts the initial condition, where the colour corresponds to  $|\mathbf{n} \cdot \mathbf{r}|$  with  $\mathbf{r} = \mathbf{x}/|\mathbf{x}|$ , i.e. the radial unit vector (see §5b). The stripes in the initial condition form a spiral on the spherical boundary running top to bottom, with spacing inversely proportional to  $\tau_0$ . Moreover, figures 4 and 5 show the final equilibrium state of  $Q$ , corresponding to a local minimizer, for both homeotropic and planar degenerate anchoring for a range of twist values  $\tau_0$ .

For the second shell, we set  $\Omega = \Omega_{\text{shell},1} := \mathcal{B}(\mathbf{0}, 1) \setminus \overline{\mathcal{B}}(\mathbf{p}, 0.9)$ , where  $\mathbf{p} = (0, 0, 0.05)^\dagger$ , i.e. an off-centred annulus. Our mesh size was again set to  $h = 0.02$ . We used the same initial condition here as in (5.4). Figure 6 shows the initial condition, as well as the final equilibrium state, for a range of twist values.

We also performed another set of numerical experiments for the first shell,  $\Omega = \Omega_{\text{shell},0}$ , but with the initial condition set to  $Q_0$  in (5.3). Figure 7 shows the initial condition, as well as the final equilibrium state, for a range of twist values. We omitted the case of  $\tau_0 = 0$ , since the results were not appreciably different from the previous experiments.

## (ii) Results

We begin with the centred shell  $\Omega_{\text{shell},0}$  and initial condition (5.4). Table 2 lists the (non-dimensional) energies of the initial condition for each  $\tau_0$  compared to the energies of the equilibrium state (a local minimizer), for both homeotropic and planar degenerate anchoring.

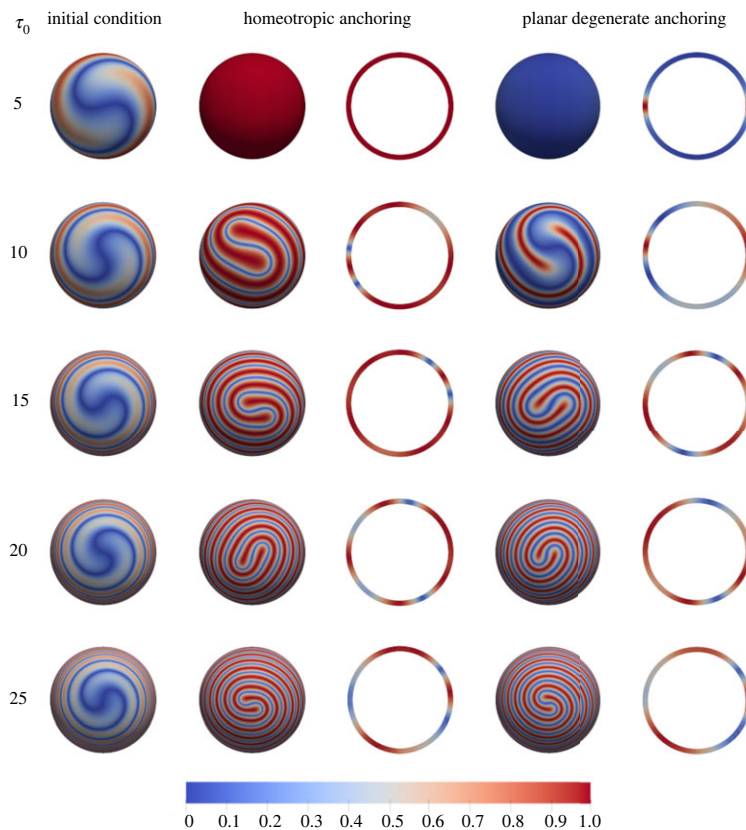


**Figure 5.** Centred shell ( $\Omega_{\text{shell},0}$ ), top view (viewing the  $xy$  plane) (S5d, part (ii)). Similar format to figure 4; the slices are parallel to the view plane.

Figures 4 and 5 (middle column) depict the final equilibrium solutions with homeotropic anchoring, where the spiral stripe pattern has a slight undulation. Moreover, the spirals meet as two ‘fingers’ at the poles of the shell. The slice views show that the spiral pattern persists through the shell’s thickness. For  $\tau_0 = 5$ , instead of a stripe pattern, the director  $\mathbf{n}$  is radial pointing outward from the origin, because the anchoring strength outweighs the twist effect.

For the planar degenerate anchoring case (figures 4 and 5 (right column)), similar striped patterns are present in the equilibrium solutions for each twist value. We note that the transition between stripes is slightly different from the homeotropic case (as for the slab). For  $\tau_0 = 5$ , the director field is mainly tangential, except for two ‘poles’ where the director becomes normal to the surface of the shell. Again, this is because the anchoring constants outweigh the twist.

Each simulation time ranged from 0 to 26 h for the homeotropic case, and 0 to 11 h for the planar degenerate case (with an exception for  $\tau_0 = 10$  which took nearly 20 h). In general, higher twist correlates with longer simulation times, and the planar degenerate case took longer than the homeotropic case.

Next, we consider the off-centred shell  $\Omega_{\text{shell},1}$  and initial condition (5.4). Table 3 lists the (non-dimensional) energies of the initial condition for each  $\tau_0$  compared to the energies of the equilibrium state (a local minimizer), for both homeotropic and planar degenerate anchoring.

Figure 6 depicts the final equilibrium solutions for both homeotropic and planar degenerate anchoring, which show similar stripe patterns as for the previous centred shell. But there are some differences. For  $\tau_0 = 5$  with planar degenerate anchoring, the two ‘poles’ where the director becomes normal to the surface are shifted down towards the thicker part of the shell. For  $\tau_0 = 10$  and homeotropic anchoring, the stripe pattern is absent at the top (thinnest) part of the shell;

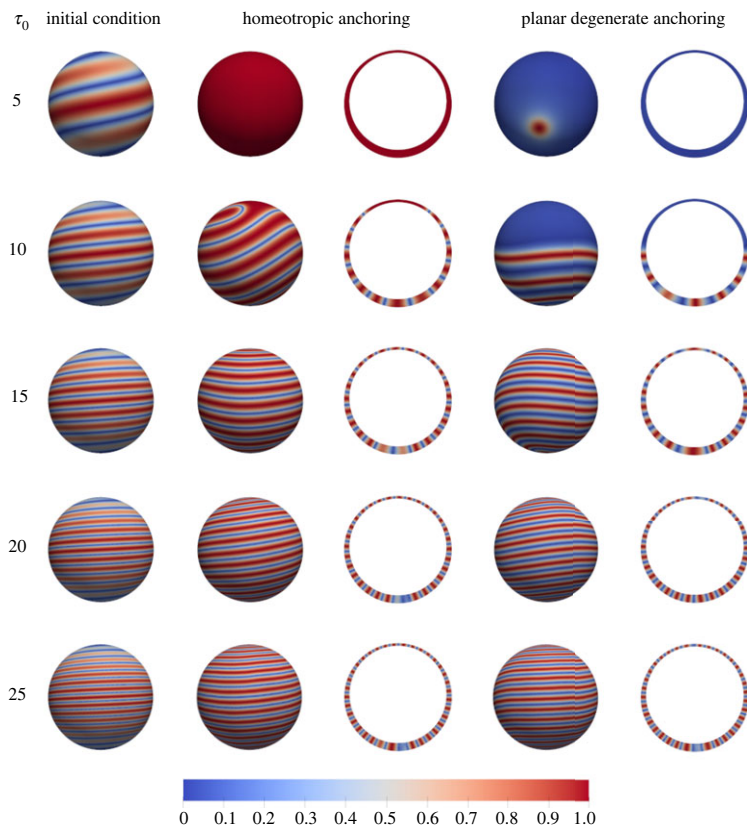


**Figure 6.** Off-centred shell ( $\Omega_{\text{shell},1}$ ), front view (viewing the yz plane) (S5d, part (ii)). Similar format to figure 4.

for planar degenerate, the spiral pattern is only present on the lower (thicker) half of the shell. For higher twists, the spiral patterns are similar to the previous (centred) shell. This is due to the interplay of the anchoring strength and the twist. Basically, there is not enough ‘room’ in the thinnest part of the shell to develop a twist of the director field if  $\tau_0$  is not sufficiently large. Each simulation time ranged from 0 to 24 h for the homeotropic case, and 2 to 80 h for the planar degenerate case. In general, higher twist correlates with longer simulation times, and the planar degenerate case took longer than the homeotropic case. For example, with  $\tau_0 = 0$ , it took around 30 min for the homeotropic case, and 32 h for the planar degenerate case.

We now reconsider the centred shell  $\Omega_{\text{shell},0}$  but with the initial condition (5.3). Table 4 lists the (non-dimensional) energies of the initial condition for each  $\tau_0$  compared to the energies of the equilibrium state (a local minimizer), for both homeotropic and planar degenerate anchoring.

Figure 7 depicts the final equilibrium solutions for both homeotropic and planar degenerate anchoring, which show similar stripe patterns as before. However, the stripe patterns break away from being a spiral in some cases. For instance, with homeotropic anchoring and  $\tau_0 = 15, 20$ , we see multiple triple junctions of the blue region. In addition, we see similar triple junctions for the planar degenerate anchoring with  $\tau_0 = 15$ . The  $\tau_0 = 10$  case (planar degenerate) exhibits a somewhat bizarre hexagonal/pentagonal pattern with a slightly lower energy than the minimizer in figures 4 and 5 ( $\mathcal{E} = -66.795$  versus  $\mathcal{E} = -62.482$ ). Despite redoing this case with a finer mesh size of  $h = 0.015$ , the pattern persisted (with a final energy of  $\mathcal{E} = -68.244$ ), suggesting that this may represent a true minimizer. The other cases exhibited a similar spiral pattern as before. Each simulation took from 1 to 33 h for the homeotropic case, and 4 to 14 h for the planar degenerate case, with the latter case generally taking a shorter time than the former.

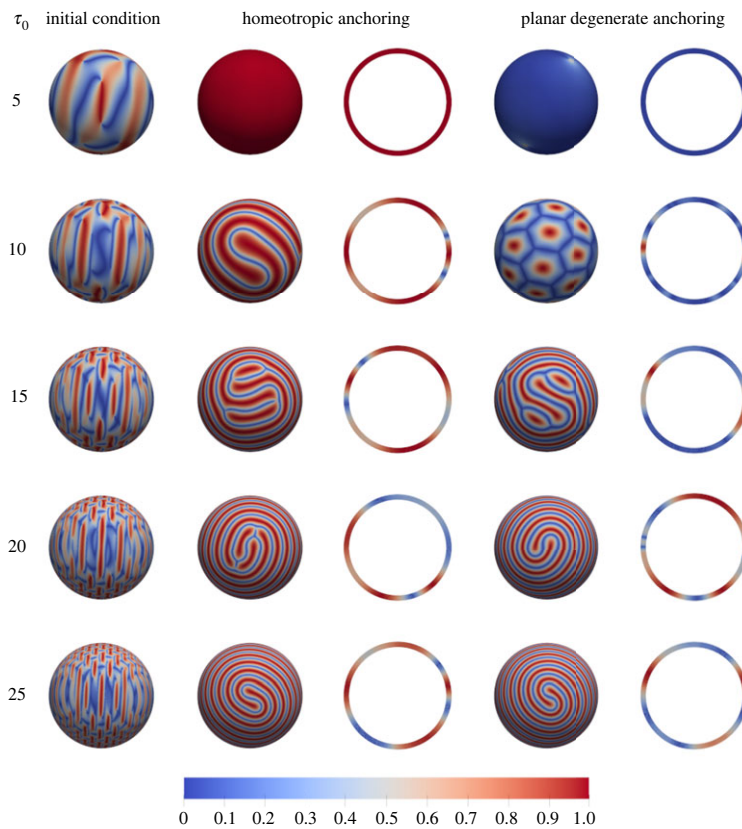


**Figure 7.** Centred shell ( $\mathcal{L}_{\text{shell},0}$ ) with oscillatory initial condition, front view (viewing the yz plane) (S5d, part (ii)). Similar format to figure 4.

**Table 2.** Energies for the centred shell ( $\mathcal{L}_{\text{shell},0}$ ) in figures 4 and 5.

$\tau_0$	homeotropic anchoring		planar degenerate anchoring	
	initial energy	final energy	initial energy	final energy
0	1.23566209	1.23349847	56.94106826	51.13769725
5	60.49129983	1.23349741	12.23300007	-13.13068291
10	21.34536007	-33.76001607	-26.81216759	-62.48198396
15	-36.59992963	-151.97707415	-84.58904161	-185.01096392
20	-103.25794942	-348.22427414	-151.0115368	-384.49961726
25	-166.11557298	-639.23581796	-213.57414074	-677.04411588

### (e) Comments on computing minimizers

We demonstrate the ramifications of theorem 4.2, which has a mesh size restriction, on the form of discrete minimizers. Because of the non-convex terms in the energy, i.e. the double well and cholesteric term, the choice of mesh size affects more than just the resolution of the features of the minimizer  $Q$ . Indeed, too coarse a mesh can yield discrete minimizers that contain numerical artifacts, i.e. the ‘minimizer’ may be very far from a true minimizer of the continuous problem. Figure 8a shows two simulations, one for the slab and one for shell, that illustrate how these numerical artifacts may manifest. In other words, when the mesh size is too large, the energy landscape of the discrete energy functional may contain artificial minima, so the gradient flow finds a different minimizer with a very different structure.

**Table 3.** Energies for the off-centred shell ( $\Omega_{\text{shell},1}$ ) in figure 6.

$\tau_0$	homeotropic anchoring		planar degenerate anchoring	
	initial energy	final energy	initial energy	final energy
0	1.34958562	1.26765658	56.95232872	1.56772626
05	60.4884546	1.24104888	12.23023189	-13.2233694
10	21.30137144	-34.07603296	-26.85588133	-64.03286781
15	-36.81485612	-149.89711829	-84.80477055	-182.77158029
20	-103.91110362	-342.9675383	-151.66656546	-379.13022842
25	-167.63544101	-630.70950725	-215.09203743	-668.63027357

**Table 4.** Energies for the centred shell ( $\Omega_{\text{shell},0}$ ), with oscillatory initial condition, in figures 7.

$\tau_0$	homeotropic anchoring		planar degenerate anchoring	
	initial energy	final energy	initial energy	final energy
5	107.21684588	1.23349885	65.88019321	-12.85142139
10	143.69128926	-33.21147874	103.37532314	-66.79504813
15	198.33754579	-151.71328798	158.2365114	-185.18312273
20	269.46171783	-348.4203652	229.41729719	-384.3815465
25	352.2492802	-639.0239269	312.42189391	-676.81099557

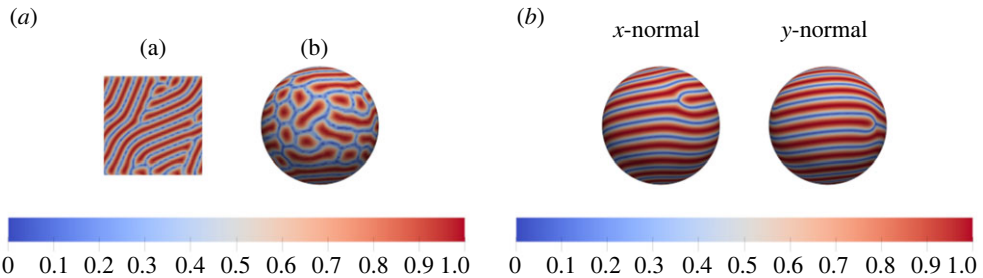


**Figure 8.** (a) Equilibrium states when the mesh size is not small enough (S5e). Example (a) shows an energy minimizer, with  $\mathcal{E} = -213.62$ , for the large slab with the oscillatory initial condition and  $\tau_0 = 20$ , but with a mesh size of 0.05 (cf. figure 3 (homeotropic), with  $\mathcal{E} = -254.84$ , that used a mesh size of 0.02). Clearly, the period of the stripes in figure 3 is much smaller than in (a) (to be exact, the period here is around 0.576). Example (b) shows a minimizer, with  $\mathcal{E} = -757.69$ , for the centred shell with the periodic initial condition and  $\tau_0 = 25$ , but with a mesh size of 0.05 and a shell thickness of 0.2 (cf. figure 4 (homeotropic), with  $\mathcal{E} = -639.24$ , that used a mesh size of 0.02 and a thickness of 0.1). (b) Different equilibrium states with mismatched initial condition (S5e). We consider a centred shell with homeotropic anchoring and a twist of  $\tau_0 = 15$  (recall figure 4 (homeotropic)). However, we use a periodic initial condition consistent with  $\tau_0 = 25$  (see far left col. in figure 4), i.e. more stripes than the minimizer should have. The computed minimizer has energy  $\mathcal{E} = -151.78$ , compared to  $\mathcal{E} = -151.98$  in figure 4 (homeotropic), and contains two triple junctions not present in the previous simulation.

We also consider another type of perturbation of the initial condition in figure 8b. Here, a centred shell, with homeotropic anchoring, is considered with  $\tau_0 = 15$ , but the initial condition corresponds to  $\tau_0 = 25$ , i.e. more tightly packed stripes. Because of this mismatch of the initial condition, the simulation took approximately 1 week to ‘unwind’ the extra twist in the initial condition to arrive at a minimizer with  $\tau_0 = 15$ . Moreover, the gradient flow obtained a different minimizer with a stripe pattern having two triple junctions, as opposed to figure 4 which had no triple junctions.

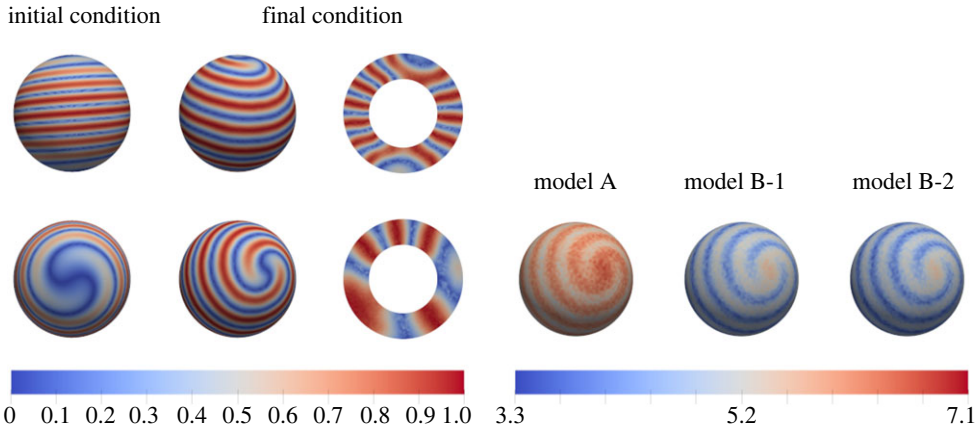


**Figure 9.** (a) Results from the simulation of Model A (S5f). Both a front view (viewing the  $yz$  plane) and a top view (viewing the  $xy$  plane) are shown, with a view of the initial condition and final state (both outside view and slice are shown). Models B-1 and B-2 had visually indistinguishable patterns. (b) Results from the simulation of Models A, B-1, B-2 (S5f), except viewing the largest eigenvalue  $\bar{\lambda} = \max\{\lambda_i\}_{i=1}^3$  of the energy minimizing  $Q$ . We have Model A (our formulation), Model B-1, (their formulation with their inconsistent  $s_0$ ), and Model B-2 (their formulation with a consistent  $s_0$ ).

### (f) Other cholesteric model

We attempted to reproduce a result of Lavrentovich and Tran in [12, Fig. 6], which models a cholesteric shell with outer radius  $0.42 \mu\text{m}$  and inner radius  $0.24 \mu\text{m}$ . From this, we choose the characteristic length  $\xi = 0.42 \mu\text{m}$ .

The dimensional parameters used are for the 5CB LC, which can be found in [29]. The double well constants are  $a_2 = 0.172 \times 10^6 \text{ J m}^{-3}$ ,  $a_3 = 2.12 \times 10^6 \text{ J m}^{-3}$  and  $a_4 = 1.73 \times 10^6 \text{ J m}^{-3}$ . Following §2c, we then calculate  $c_0 = 0.038362224 \times 10^6 \text{ J m}^{-3}$ , and divide the double well coefficients by  $c_0$  to obtain the non-dimensional double well:

$$a_0 = 1.0, \quad a_2 = 4.4835774, \quad a_3 = 55.262698, \quad a_4 = 45.096447,$$

which gives  $s_0 = 0.7992969$ .

For the elastic coefficients (for 5CB in [29]), we have  $\check{\ell}_1 = \check{\ell}_2 = 4 \times 10^{-11} \text{ J m}^{-1}$ ,  $\check{\ell}_{24} = 0$ . Since  $\check{\ell}_{24} = 0$ , this corresponds, via the mapping of the constants in §2d, to  $\ell_1 = \ell_2 = 4 \times 10^{-11} \text{ J m}^{-1}$ ,  $\ell_3 = -4 \times 10^{-11} \text{ J m}^{-1}$ . From here, we choose  $\ell_m = 4 \times 10^{-11} \text{ J m}^{-1}$  and divide by  $\ell_m$  to obtain  $\ell_1 = \ell_2 = 1$ ,  $\ell_3 = -1$ . Note that the inequalities in (3.2) are not strictly satisfied in this case. We also have a cholesteric pitch of  $p = 0.18 \mu\text{m}$ , and so the non-dimensional twist is  $\tau_0 = 14.660766$ . The anchoring condition is planar degenerate with  $w_0 = 0$ ,  $w_1 = 4 \times 10^{-4} \text{ J m}^{-2}$ ,  $w_2 = 8 \times 10^{-4} \text{ J m}^{-2}$ . Multiplying the first two by  $\xi/\ell_m$ , we obtain  $w_0 = 0$ ,  $w_1 = 4.2$ . Finally, using the formulae  $\eta = \sqrt{\ell_m/(c_0\xi^2)}$  and  $\omega = \ell_m/(w_2\xi)$ , we have that  $\eta = 0.07688273$  and  $\omega = 0.11904762$ .

We ran simulations for the above parameters using the following three models: A, B-1, B-2. Model A is given in (2.3) (see [9,10,29]), and model B-1 is the cholesteric model in [11] and discussed in §2d. Since  $s_0$  is inconsistent with their *effective* double well  $\tilde{\psi}$  (see §2d, part (ii), and the discussion about the extra  $\text{tr}(Q^2)$  term), we ran the simulation for a model B-2, which is identical to B-1, except that we replace  $s_0$  with the correct global minimum  $\tilde{s}_0$  for  $\tilde{\psi}$ .

The energy results of these simulations are found in table 5, and the results of the simulation using model A are found in figure 9a, which does not exactly match the result in [12, fig. 6]. Their method uses a conjugate gradient method which is different from our minimization scheme, i.e. their method travels along a different path in the energy landscape so finds a different local minimizer.

We do not give the visualization of the other two models (B-1, B-2), because they look *nearly identical* to Model A. We suspect this is due to the cholesteric twist having a dominant effect. It

**Table 5.** Energies for the model comparisons in figure 9 (§5f).

model	initial energy	final energy
A	−196.83349123	−479.36144656
B-1	310.00570697	185.52404418
B-2	365.134880212	183.86282819

should be noted, however, that models A and B-1, B-2 differ greatly in their final energies, as well as in the values of the maximum eigenvalue  $\bar{\lambda}$  of  $Q$ , the latter of which is shown in figure 9b. We emphasize that, due to the energetic differences, if other physical effects were to be coupled to the LC (e.g. electro-static effects), then the models would most likely give vastly different equilibrium states. In addition, if the twist parameter is sufficiently large, then the effective bulk potential (recall §2d(ii)) will favour an isotropic state, which is not consistent with cholesteric LC behaviour [11,12,17].

It took approximately 2 h to simulate model A, while it took about 40 min to simulate models B-1 and B-2. The mesh size used was 0.04285714.

## 6. Conclusion

The first part of this paper gives an overview of the LdG model [9,10,29] for nematic LCs, with cholesteric effects, and connects it to a slightly different cholesteric model in [11]. We then presented a gradient flow and numerical scheme for the cholesteric LdG model, while noting important time-step restrictions to have an energy decreasing algorithm. Moreover, we gave a mesh size restriction that ensures that discrete minimizers are approximate versions of isolated, true minimizers.

Using our gradient flow, we compute (local) minimizers with an adaptive time-stepping strategy to reduce the computation time. This produced several numerical simulations that illustrate the rich behaviour of the cholesteric LdG model. For both slab and shell geometries, the minimizer has regular stripe patterns that are affected by the domain shape. Specifically, the off-centred shell has a very different minimizer than the centred shell for intermediate values of the twist  $\tau_0$ . We also demonstrate that our gradient flow scheme can compute different (local) minimizers for the same set of parameters but depending on the initial condition. Some of the simulations show perturbed stripe patterns that exhibit ‘triple junctions’ of the stripe and are due to using initial conditions with a high spatial frequency. All of these (equilibrium) stripe patterns are in line with known experiments for cholesteric LCs (for instance, see [48,49] for examples with thin slab geometries, and [11,12,16,17] for shell geometries).

We also gave examples of how artificial solutions may arise if the mesh size is not small enough, i.e. the computed minimizer may exhibit discrete artefacts. Furthermore, we showed that the two cholesteric models exhibit very different energies, though the computed solution may still have a very similar configuration of the director  $\mathbf{n}$ .

The results of this paper should help inform LC computational scientists about potential pitfalls in the simulation of the cholesteric LdG model and lead to more robust numerical predictions of cholesteric LC physics.

**Data accessibility.** Code is available at the following Zenodo records: <https://zenodo.org/records/10929107> [50]; <https://zenodo.org/records/10929109> [51]; <https://zenodo.org/records/10929113> [52].

**Declaration of AI use.** Declaration of AI use We have not used AI-assisted technologies in creating this article.

**Authors' contributions.** A.L.H.: conceptualization, data curation, formal analysis, investigation, methodology, project administration, software, visualization, writing—original draft, writing—review and editing; S.W.W.: conceptualization, formal analysis, funding acquisition, methodology, project administration, supervision, writing—original draft, writing—review and editing.

All authors gave final approval for publication and agreed to be held accountable for the work performed therein.

**Conflict of interest declaration.** We declare we have no competing interests.

**Funding.** No funding has been received for this article.

## Appendix A

### (a) Proof of theorem 3.1

*Proof of theorem 3.1.* We start with the following inequality for any  $P, T \in \mathbf{V}$  (recall that  $a_2, a_3, a_4 > 0$ ):

$$\begin{aligned} (T, D^2\psi(P)T)_\Omega &= -a_2\|T\|_{0,\Omega}^2 - 2a_3(PT, T)_\Omega + 2a_4(P : T, P : T)_\Omega + a_4(|T|^2, |P|^2)_\Omega \\ &\geq -a_2\|T\|_{0,\Omega}^2 - (a_3\delta)(|T|^2, |P|^2)_\Omega - (a_3/\delta)\|T\|_{0,\Omega}^2 + a_4(|T|^2, |P|^2)_\Omega \\ &= -\left(\frac{a_2 + a_3^2}{a_4}\right)\|T\|_{0,\Omega}^2 = -a'\|T\|_{0,\Omega}^2, \end{aligned} \quad (\text{A } 1)$$

by choosing  $\delta = a_4/a_3$ , where  $a' = a_2 + a_3^2/a_4$ . Similarly, we have

$$\begin{aligned} (T, D^2\phi(P)T)_\Gamma &= \left(\frac{-2s_0^2}{3}\right)\|T\|_{0,\Gamma}^2 + 2(P : T, P : T)_\Gamma + (|T|^2, |P|^2)_\Gamma \\ &\geq \left(\frac{-2s_0^2}{3}\right)\|T\|_{0,\Gamma}^2 = -s'\|T\|_{0,\Gamma}^2, \end{aligned} \quad (\text{A } 2)$$

where  $s' = 2s_0^2/3$ . Next, setting  $S_{k+1} := Q_{k+1} - Q_k$ , we have the identity

$$a(Q_k, Q_k) = a(Q_{k+1}, Q_{k+1}) + a(S_{k+1}, S_{k+1}) - 2a(S_{k+1}, Q_{k+1}). \quad (\text{A } 3)$$

Note also that, substituting  $P = S_{k+1} := Q_{k+1} - Q_k$  into (3.10) and (3.7), we have

$$\begin{aligned} \delta t^{-1}(S_{k+1}, S_{k+1})_{\delta t} &= -a(Q_{k+1}, S_{k+1}) - \left(\frac{1}{\eta^2}\right)(D\psi(Q_{k+1}), S_{k+1})_\Omega \\ &\quad - \left(\frac{1}{\omega}\right)(D\phi(Q_{k+1}), S_{k+1})_\Gamma + l_{\text{rhs}}(S_{k+1}). \end{aligned} \quad (\text{A } 4)$$

Now use a Taylor expansion of  $\psi(Q_k)$  and  $\phi(Q_k)$  about  $Q_{k+1}$ , i.e. set  $\bar{Q}(s) := (1-s)Q_{k+1} + sQ_k$ , and for some  $s_1, s_2 \in (0, 1)$ , we obtain from (3.6) combined with (A 1), (A 2), (A 3):

$$\begin{aligned} \mathcal{E}[Q_k] &= \left(\frac{1}{2}\right)a(Q_k, Q_k) + \left(\frac{1}{\eta^2}\right)(\psi(Q_{k+1}), 1)_\Omega + \left(\frac{1}{\omega}\right)(\phi(Q_{k+1}), 1)_\Gamma \\ &\quad - l_{\text{rhs}}(Q_{k+1}) + l_{\text{rhs}}(S_{k+1}) - \left(\frac{1}{\eta^2}\right)(D\psi(Q_{k+1}), S_{k+1})_\Omega \\ &\quad - \left(\frac{1}{\omega}\right)(D\phi(Q_{k+1}), S_{k+1})_\Gamma + \left(\frac{1}{(2\eta^2)}\right)(S_{k+1}, D^2\psi(\bar{Q}(s_1))S_{k+1})_\Omega \\ &\quad + \left(\frac{1}{(2\omega)}\right)(S_{k+1}, D^2\phi(\bar{Q}(s_2))S_{k+1})_\Gamma \end{aligned}$$

$$\begin{aligned}
&\geq \left(\frac{1}{2}\right) a(Q_{k+1}, Q_{k+1}) + \left(\frac{1}{\eta^2}\right) (\psi(Q_{k+1}), 1)_{\Omega} + \left(\frac{1}{\omega}\right) (\phi(Q_{k+1}), 1)_{\Gamma} \\
&\quad - l_{\text{rhs}}(Q_{k+1}) + \left(\frac{1}{2}\right) a(S_{k+1}, S_{k+1}) - a(S_{k+1}, Q_{k+1}) + l_{\text{rhs}}(S_{k+1}) \\
&\quad - \left(\frac{1}{\eta^2}\right) (D\psi(Q_{k+1}), S_{k+1})_{\Omega} - \left(\frac{1}{\omega}\right) (D\phi(Q_{k+1}), S_{k+1})_{\Gamma} \\
&\quad - \left(\frac{1}{\eta^2}\right) \left(\frac{a'}{2}\right) \|S_{k+1}\|_{0,\Omega}^2 - \left(\frac{1}{\omega}\right) \left(\frac{s'}{2}\right) \|S_{k+1}\|_{0,\Gamma}^2.
\end{aligned}$$

We then substitute (A 4) into the above line and use (3.6) again to see that

$$\begin{aligned}
\mathcal{E}[Q_k] &\geq \mathcal{E}[Q_{k+1}] + \delta t^{-1} (S_{k+1}, S_{k+1})_{\delta t} - \left(\frac{1}{\eta^2}\right) \left(\frac{a'}{2}\right) \|S_{k+1}\|_{0,\Omega}^2 - \left(\frac{1}{\omega}\right) \left(\frac{s'}{2}\right) \|S_{k+1}\|_{0,\Gamma}^2 \\
&= \mathcal{E}[Q_{k+1}] + \left(\frac{1}{\eta^2}\right) \left(\frac{1}{\delta} t - \frac{a'}{2}\right) \|S_{k+1}\|_{0,\Omega}^2 + \left(\frac{1}{\omega}\right) \left(\frac{1}{\delta} t - \frac{s'}{2}\right) \|S_{k+1}\|_{0,\Gamma}^2 \geq \mathcal{E}[Q_{k+1}],
\end{aligned}$$

provided that  $\delta t \leq 2/\max\{a', s'\}$ . ■

## (b) Proof of theorem 4.2

To facilitate the proof of theorem 4.2, we first give several intermediate results.

**Lemma A.1 (Gårding's inequality).** *There exists  $k \geq 0$  such that*

$$a(P, P) + k\|P\|_{0,\Omega}^2 \geq \frac{\alpha_1}{2}\|P\|_{1,\Omega}^2, \quad \forall P \in V,$$

where  $\alpha_1$  is the constant found in (3.3).

*Proof.* We follow the proof found in [45], with modifications for our particular case. First, note the coercivity result from (3.3):  $a_e(P, P) + a_s(P, P) \geq \alpha_1\|P\|_{1,\Omega}^2$ . Next, recall (3.4) and note that  $|\varepsilon_{ikl}(P_{jk,l}, P_{ij})_{\Omega}| \leq \sqrt{27}|P|_{1,\Omega}\|P\|_{0,\Omega}$  (where  $|P|_{1,\Omega}^2 := \|\nabla P\|_{0,\Omega}^2$  denotes the  $H^1(\Omega)$  semi-norm), and using a weighted Young's inequality, we have

$$\begin{aligned}
a(P, P) + k\|P\|_{0,\Omega}^2 &\geq \alpha_1\|P\|_{1,\Omega}^2 + 4\ell_1\tau_0\varepsilon_{ikl}(P_{jk,l}, P_{ij})_{\Omega} + k\|P\|_{0,\Omega}^2 \\
&\geq \alpha_1\|P\|_{1,\Omega}^2 - (4\ell_1\sqrt{27})\tau_0|P|_{1,\Omega}\|P\|_{0,\Omega} + k\|P\|_{0,\Omega}^2 \\
&\geq \alpha_1|P|_{1,\Omega}^2 - 2\ell_1\sqrt{27}\tau_0\delta|P|_{1,\Omega}^2 - 2\ell_1\sqrt{27}\tau_0\delta^{-1}\|P\|_{0,\Omega}^2 + (k + \alpha_1)\|P\|_{0,\Omega}^2 \\
&= (\alpha_1 - 2\ell_1\sqrt{27}\tau_0\delta)|P|_{1,\Omega}^2 + (k + \alpha_1 - 2\ell_1\sqrt{27}\tau_0\delta^{-1})\|P\|_{0,\Omega}^2 \\
&\geq \left(\frac{\alpha_1}{2}\right)\|\nabla P\|_{0,\Omega}^2 + \left(\frac{\alpha_1}{2}\right)\|P\|_{0,\Omega}^2.
\end{aligned}$$

Finally, by choosing  $\delta = \alpha_1/(4\ell_1\tau_0\sqrt{27})$  the result follows by assuming:

$$k = \max \left[ \left( \frac{216\ell_1^2\tau_0^2}{\alpha_1} - \frac{\alpha_1}{2} \right), 0 \right]. \quad (\text{A5})$$

**Lemma A.2.** *The following inequality holds:*

$$\frac{\alpha_1}{4}\|Q - Q_h\|_{1,\Omega}^2 \leq c_1\|Q - Q_h\|_{1,\Omega}\|Q - P_h\|_{1,\Omega} + \tilde{k}\|Q - Q_h\|_{0,\Omega}^2, \quad \forall P_h \in V_h,$$

where  $c_1$  and  $\tilde{k}$  are nonnegative constants, and  $Q, Q_h$  are defined in theorem 4.2. ■

*Proof.* First, observe that, by subtracting (4.3) from (3.7) (choosing  $P = P_h \in \mathbf{V}_h$ ), we obtain

$$a(Q - Q_h, P_h) + \left(\frac{1}{\eta^2}\right) (D\psi(Q) - D\psi(Q_h), P_h)_\Omega + \left(\frac{1}{\omega}\right) (D\phi(Q) - D\phi(Q_h), P_h)_\Gamma = 0, \quad (\text{A } 6)$$

for all  $P_h \in \mathbf{V}_h$ . Secondly, for all symmetric tensors  $Q_1, Q_2, P$ , note that

$$\begin{aligned} (D\psi(Q_1) - D\psi(Q_2)) : P &= -a_2(H : P) - a_3(Q_1^2 - Q_2^2) : P + a_4(|Q_1|^2 Q_1 - |Q_2|^2 Q_2) : P \\ &= -a_2(H : P) - a_3(H : (Q_1 + Q_2)P) \\ &\quad + \frac{a_4}{2} [(|Q_1|^2 + |Q_2|^2)H : P + (H : (Q_1 + Q_2))(Q_1 + Q_2) : P] \\ &= H : \left( -a_2 \mathcal{I} - a_3(Q_1 + Q_2)\mathcal{I} + \frac{a_4}{2} [(|Q_1|^2 + |Q_2|^2)\mathcal{I} \right. \\ &\quad \left. + (Q_1 + Q_2) \otimes (Q_1 + Q_2)] \right) P =: H : \Theta(Q_1, Q_2)P, \end{aligned}$$

where  $H = Q_1 - Q_2$  and  $\mathcal{I}$  is the 4-tensor identity. Similarly, we have

$$\begin{aligned} (D\phi(Q_1) - D\phi(Q_2)) : P &= -\frac{2s_0}{3}H : P + (|Q_1|^2 Q_1 - |Q_2|^2 Q_2) : P \\ &= -\frac{2s_0^2}{3}H : P + \left(\frac{1}{2}\right) [(|Q_1|^2 + |Q_2|^2)H : P + (P : (Q_1 + Q_2))(Q_1 + Q_2) : H] \\ &= H : \left( -\frac{2s_0^2}{3}\mathcal{I} + \left(\frac{1}{2}\right) [(|Q_1|^2 + |Q_2|^2)\mathcal{I} \right. \\ &\quad \left. + (Q_1 + Q_2) \otimes (Q_1 + Q_2)] \right) P =: H : \Xi(Q_1, Q_2)P. \end{aligned}$$

Note also that these tensors obey the inequality

$$\begin{aligned} (P, \Theta(Q_1, Q_2)P)_\Omega &\geq \int_\Omega -a_2|P|^2 - a_3(P : (Q_1 + Q_2)P) + \left(\frac{a_4}{2}\right) (|Q_1|^2 + |Q_2|^2)|P|^2 \\ &\geq \int_\Omega -a_2|P|^2 - \left(\frac{a_3\delta^{-1}}{2}\right) |P|^2 - \left(\frac{a_3\delta}{2}\right) |Q_1 + Q_2|^2|P|^2 \\ &\quad + \left(\frac{a_4}{2}\right) (|Q_1|^2 + |Q_2|^2)|P|^2 \\ &\geq \int_\Omega -a_2|P|^2 - \left(\frac{a_3\delta^{-1}}{2}\right) |P|^2 - (a_3\delta)(|Q_1|^2 + |Q_2|^2)|P|^2 \\ &\quad + \left(\frac{a_4}{2}\right) (|Q_1|^2 + |Q_2|^2)|P|^2 \\ &= -\left(\frac{a_2 + a_3^2}{a_4}\right) \|P\|_{0,\Omega}^2 = -a' \|P\|_{0,\Omega}^2, \end{aligned}$$

and also

$$\begin{aligned} (P, \Xi(Q_1, Q_2)P)_\Gamma &= \int_\Gamma -\left(\frac{2s_0^2}{3}\right) |P|^2 + \left(\frac{1}{2}\right) (|Q_1|^2 + |Q_2|^2)|P|^2 + \left(\frac{1}{2}\right) ((Q_1 + Q_2) : P)^2 \\ &\geq \int_\Gamma -\left(\frac{2s_0^2}{3}\right) |P|^2 = -s' \|P\|_{0,\Gamma}^2, \end{aligned}$$

for all  $Q_1, Q_2, P$ , where we have chosen  $\delta = a_4/2a_3$ ,  $a' = a_2 + a_3^2/a_4$ , and  $s' = 2s_0^2/3$ . Then, for all  $P_h \in \mathbf{V}_h$ , we have

$$\begin{aligned} a(Q - Q_h, Q - Q_h) &= a(Q - Q_h, Q - P_h) + a(Q - Q_h, P_h - Q_h) \\ &= a(Q - Q_h, Q - P_h) - \left(\frac{1}{\eta^2}\right) (D\psi(Q) - D\psi(Q_h), P_h - Q_h)_\Omega \\ &\quad - \left(\frac{1}{\omega}\right) (D\phi(Q) - D\phi(Q_h), P_h - Q_h)_\Omega. \end{aligned}$$

Substituting  $\Theta$  and  $\Xi$  into the above, we see that

$$\begin{aligned} a(Q - Q_h, Q - Q_h) &= a(Q - Q_h, Q - P_h) - \left(\frac{1}{\eta^2}\right) (Q - Q_h, \Theta(Q, Q_h)(P_h - Q_h))_\Omega \\ &\quad - \left(\frac{1}{\omega}\right) (Q - Q_h, \Xi(Q, Q_h)(P_h - Q_h))_\Gamma \\ &= a(Q - Q_h, Q - P_h) + \left(\frac{1}{\eta^2}\right) (Q - Q_h, \Theta(Q, Q_h)(Q - P_h))_\Omega \\ &\quad + \left(\frac{1}{\omega}\right) (Q - Q_h, \Xi(Q, Q_h)(Q - P_h))_\Gamma \\ &\quad - \left(\frac{1}{\eta^2}\right) (Q - Q_h, \Theta(Q, Q_h)(Q - Q_h))_\Omega - \left(\frac{1}{\omega}\right) (Q - Q_h, \Xi(Q, Q_h)(Q - Q_h))_\Gamma \\ &\leq c_0 \|Q - Q_h\|_{1,\Omega} \|Q - P_h\|_{1,\Omega} \\ &\quad + \left(\frac{1}{\eta^2}\right) \|\Theta(Q, Q_h)\|_{0,3,\Omega} \|Q - Q_h\|_{0,6,\Omega} \|Q - P_h\|_{0,\Omega} \\ &\quad + \left(\frac{1}{\omega}\right) \|\Xi(Q, Q_h)\|_{0,\Gamma} \|Q - Q_h\|_{0,4,\Gamma} \|Q - P_h\|_{0,4,\Gamma} \\ &\quad + \frac{a'}{\eta^2} \|Q - Q_h\|_{0,\Omega}^2 + \frac{s'}{\omega} \|Q - Q_h\|_{0,\Gamma}^2, \end{aligned}$$

where  $c_0$  is the continuity constant defined in (4.6) (see [40] for details), and  $\|P\|_{0,p,\Omega}^p := (|P|^p, 1)_\Omega$ . Applying the Sobolev trace and embedding theorems, with induced constants  $\beta_1, \beta_2 > 0$ , we get

$$\begin{aligned} a(Q - Q_h, Q - Q_h) &\leq c_0 \|Q - Q_h\|_{1,\Omega} \|Q - P_h\|_{1,\Omega} \\ &\quad + \left(\frac{\beta_1}{\eta^2}\right) \|\Theta(Q, Q_h)\|_{0,3,\Omega} \|Q - Q_h\|_{1,\Omega} \|Q - P_h\|_{1,\Omega} \\ &\quad + \left(\frac{\beta_2}{\omega}\right) \|\Xi(Q, Q_h)\|_{0,\Gamma} \|Q - Q_h\|_{1,\Omega} \|Q - P_h\|_{1,\Omega} \\ &\quad + \frac{a'}{\eta^2} \|Q - Q_h\|_{0,\Omega}^2 + \frac{s'}{\omega} \|Q - Q_h\|_{0,\Gamma}^2. \end{aligned}$$

Next, by another classic trace theorem,  $\|P\|_{0,\Gamma}^2 \leq \beta_3 \|P\|_{0,\Omega} \|P\|_{1,\Omega}$  combined with a weighted inequality, we have

$$\frac{s'}{\omega} \|Q - Q_h\|_{0,\Gamma}^2 \leq \frac{(\beta_3 s')^2}{\omega^2 \alpha_1} \|Q - Q_h\|_{0,\Omega}^2 + \frac{\alpha_1}{4} \|Q - Q_h\|_{1,\Omega}^2,$$

which leads to

$$\begin{aligned} a(Q - Q_h, Q - Q_h) &\leq c_1 \|Q - Q_h\|_{1,\Omega} \|Q - P_h\|_{1,\Omega} \\ &\quad + \left(\frac{a'}{\eta^2} + \frac{(\beta_3 s')^2}{\omega^2 \alpha_1}\right) \|Q - Q_h\|_{0,\Omega}^2 + \frac{\alpha_1}{4} \|Q - Q_h\|_{1,\Omega}^2, \end{aligned}$$

where

$$c_1 := c_0 + \left(\frac{\beta_1}{\eta^2}\right) \|\Theta(Q, Q_h)\|_{0,3,\Omega} + \left(\frac{\beta_2}{\omega}\right) \|\mathcal{E}(Q, Q_h)\|_{0,\Gamma} = c_0 + \frac{\beta'_1}{\eta^2} + \frac{\beta'_2}{\omega}. \quad (\text{A } 7)$$

Now, by Gårding's inequality, we have

$$\frac{\alpha_1}{2} \|Q - Q_h\|_{1,\Omega}^2 \leq a(Q - Q_h, Q - Q_h) + k \|Q - Q_h\|_{0,\Omega}^2.$$

And so, if we combine this with the above, define  $s'' = (\beta_3 s')^2 / \alpha_1$ , and set

$$\tilde{k} = k + \frac{a'}{\eta^2} + \frac{s''}{\omega^2}, \quad (\text{A } 8)$$

then the proof is complete.  $\blacksquare$

Now we move towards an estimate in  $L^2(\Omega)$  of  $Q - Q_h$ . In order to do this, we first introduce the solution to and regularity of an adjoint problem.

**Lemma A.3.** *There exists a solution  $R \in \mathbf{V}$  to the adjoint problem*

$$a(P, R) + \left(\frac{1}{\eta^2}\right) (R, \Theta(Q, Q_h)P)_\Omega + \left(\frac{1}{\omega}\right) (R, \mathcal{E}(Q, Q_h)P)_\Gamma = (Q - Q_h, P)_\Omega, \quad \forall P \in \mathbf{V}, \quad (\text{A } 9)$$

where we assume the regularity estimate

$$\|R\|_{2,\Omega} \leq c_3 \|Q - Q_h\|_{0,\Omega}, \quad (\text{A } 10)$$

where  $\|P\|_{2,\Omega}^2 := \|\nabla^2 P\|_{0,\Omega}^2 + \|\nabla P\|_{0,\Omega}^2 + \|P\|_{0,\Omega}^2$  denotes the  $H^2(\Omega)$  norm.

*Proof.* First note the inequality

$$\begin{aligned} P : \Theta(Q, Q_h)P &= -a_2 |P|^2 - a_3 (P : (Q_1 + Q_2)P) + \left(\frac{a_4}{2}\right) ((|Q_1|^2 + |Q_2|^2)|P|^2 + (P : (Q_1 + Q_2))^2) \\ &= -a_2 |P|^2 - 2a_3 (P : \bar{Q}P) + a_4 \left(\frac{|Q_1|^2 + |Q_2|^2}{2} |P|^2 + 2(\bar{Q} : P)^2\right) \\ &\geq -a_2 |P|^2 - 2a_3 (P : \bar{Q}P) + a_4 (|\bar{Q}|^2 |P|^2 + 2(\bar{Q} : P)^2) = P : D^2 \psi(\bar{Q})P, \end{aligned}$$

as well as the inequality,

$$\begin{aligned} P : \mathcal{E}(Q, Q_h)P &= -\left(\frac{2s_0^2}{3}\right) |P|^2 + \left(\frac{1}{2}\right) ((|Q_1|^2 + |Q_2|^2)|P|^2 + (P : (Q_1 + Q_2))^2) \\ &\geq -\left(\frac{2s_0^2}{3}\right) |P|^2 + (|\bar{Q}|^2 |P|^2 + 2(\bar{Q} : P)^2) = P : D^2 \phi(\bar{Q})P, \end{aligned}$$

where  $\bar{Q} = (Q_1 + Q_2)/2$ , and where we have used the Cauchy-Schwarz and Young inequalities. From here, using (4.4), we see that

$$\begin{aligned} a(P, P) + \left(\frac{1}{\eta^2}\right) (P, \Theta(Q, Q_h)P)_\Omega + \left(\frac{1}{\omega}\right) (P, \mathcal{E}(Q, Q_h)P)_\Gamma \\ \geq a(P, P) + \left(\frac{1}{\eta^2}\right) (P, D^2 \psi(\bar{Q})P)_\Omega + (P, D^2 \phi(\bar{Q})P)_\Gamma \geq m_0 \|P\|_{1,\Omega}^2, \end{aligned}$$

showing that this problem is coercive, and so the solution to the above is guaranteed by Lax-Milgram, which also shows that  $\|R\|_{1,\Omega} \leq c \|Q - Q_h\|_{0,\Omega}$  for some constant  $c > 0$ .  $\blacksquare$

**Remark A.4.** The additional  $H^2(\Omega)$  regularity assumed in theorem 4.2 on the solution  $Q$ , as well as the additional regularity on the adjoint solution in (A 10), may be shown rigorously (given certain smoothness assumptions on  $\Omega$ ) by applying bootstrapping techniques, and combining the previous a priori estimate for  $\|R\|_{1,\Omega}$  with the theory in [53, ch. 4].

**Lemma A.5.** *The following estimate holds for the  $L^2$ -norm difference of  $Q$  and its finite-element approximation:*

$$\|Q - Q_h\|_{0,\Omega} \leq c_4 h \|Q - Q_h\|_{1,\Omega}.$$

*Proof.* Starting from (A 6), replace  $P_h$  with  $R_h \in \mathbf{V}_h$  and use  $\Theta$  and  $\mathcal{E}$  from earlier to get

$$a(Q - Q_h, R_h) + \left(\frac{1}{\eta^2}\right) (R_h, \Theta(Q, Q_h)(Q - Q_h))_\Omega + \left(\frac{1}{\omega}\right) (R_h, \mathcal{E}(Q, Q_h)(Q - Q_h))_\Gamma = 0.$$

Then, set  $P = Q - Q_h$  in (A 9) to produce an estimate for  $\|Q - Q_h\|_{0,\Omega}$

$$\begin{aligned} (Q - Q_h, Q - Q_h)_\Omega &= a(Q - Q_h, R) + \left(\frac{1}{\eta^2}\right) (R, \Theta(Q, Q_h)(Q - Q_h))_\Omega \\ &\quad + \left(\frac{1}{\omega}\right) (R, \mathcal{E}(Q, Q_h)(Q - Q_h))_\Gamma \\ &= a(Q - Q_h, R - R_h) + \left(\frac{1}{\eta^2}\right) (R - R_h, \Theta(Q, Q_h)(Q - Q_h))_\Omega \\ &\quad + \left(\frac{1}{\omega}\right) (R - R_h, \mathcal{E}(Q, Q_h)(Q - Q_h))_\Gamma \\ &\leq a(Q - Q_h, R - R_h) \\ &\quad + \left(\frac{1}{\eta^2}\right) \|\Theta(Q, Q_h)\|_{0,3,\Omega} \|R - R_h\|_{0,6,\Omega} \|Q - Q_h\|_{0,\Omega} \\ &\quad + \left(\frac{1}{\omega}\right) \|\mathcal{E}(Q, Q_h)\|_{0,\Gamma} \|R - R_h\|_{0,4,\Gamma} \|Q - Q_h\|_{0,4,\Gamma}. \end{aligned}$$

We apply the Sobolev trace and embedding theorems to the above line and obtain that

$$\begin{aligned} (Q - Q_h, Q - Q_h)_\Omega &\leq a(Q - Q_h, R - R_h) \\ &\quad + \left(\frac{\beta_1}{\eta^2}\right) \|\Theta(Q, Q_h)\|_{0,3,\Omega} \|R - R_h\|_{1,\Omega} \|Q - Q_h\|_{1,\Omega} \\ &\quad + \left(\frac{\beta_2}{\omega}\right) \|\mathcal{E}(Q, Q_h)\|_{0,\Gamma} \|R - R_h\|_{1,\Omega} \|Q - Q_h\|_{1,\Omega} \\ &\leq c_0 \|Q - Q_h\|_{1,\Omega} \|R - R_h\|_{1,\Omega} + \left(\frac{\beta_1}{\eta^2}\right) \|\Theta(Q, Q_h)\|_{0,3,\Omega} \\ &\quad + \left(\frac{\beta_2}{\omega}\right) \|\mathcal{E}(Q, Q_h)\|_{0,\Gamma} \|Q - Q_h\|_{1,\Omega} \|R - R_h\|_{1,\Omega} \\ &= c_1 \|Q - Q_h\|_{1,\Omega} \|R - R_h\|_{1,\Omega}, \end{aligned}$$

for all  $R_h \in \mathbf{V}_h$ , where  $\beta_1, \beta_2 > 0$  are constants induced from the trace and embedding theorems, and  $c_1$  is the same as in (A 7). We then note that  $\inf_{P_h \in \mathbf{V}_h} \|P - P_h\|_{1,\Omega} \leq c_2 h |P|_{2,\Omega}$  for all  $P \in H^2(\Omega)$  (see [45], for instance), for some constant  $c_2 > 0$ , where  $|P|_{2,\Omega}^2 := \|\nabla^2 P\|_{0,\Omega}^2$  is the  $H^2(\Omega)$  seminorm. So, we can choose  $R_h$  such that by this estimate as well as (A 10), we obtain

$$(Q - Q_h, Q - Q_h)_\Omega \leq c_1 c_2 h \|Q - Q_h\|_{1,\Omega} |R|_{2,\Omega} \leq c_1 c_2 c_3 h \|Q - Q_h\|_{1,\Omega} \|Q - Q_h\|_{0,\Omega}.$$

Dividing everything by  $\|Q - Q_h\|_{0,\Omega}$ , we obtain

$$\|Q - Q_h\|_{0,\Omega} \leq c_4 h \|Q - Q_h\|_{1,\Omega}, \tag{A 11}$$

where  $c_4 := c_1 c_2 c_3$  and we are done. ■

*Proof of theorem 4.2.* Combining lemma A.2 with lemma A.5, we obtain the following for all  $P_h \in \mathbf{V}_h$ :

$$\begin{aligned} \frac{\alpha_1}{4} \|Q - Q_h\|_{1,\Omega}^2 &\leq c_1 \|Q - Q_h\|_{1,\Omega} \|Q - P_h\|_{1,\Omega} + \tilde{k} \|Q - Q_h\|_{0,\Omega}^2 \\ &\leq c_1 \|Q - Q_h\|_{1,\Omega} \|Q - P_h\|_{1,\Omega} + \tilde{k}(c_1 c_2 c_3)^2 h^2 \|Q - Q_h\|_{1,\Omega}^2. \end{aligned}$$

Moving the last term to the left-hand side and then dividing by  $\|Q - Q_h\|_{1,\Omega}$ :

$$\left(\frac{\alpha_1}{4} - \tilde{k}(c_1 c_2 c_3)^2 h^2\right) \|Q - Q_h\|_{1,\Omega} \leq c_1 \|Q - P_h\|_{1,\Omega}.$$

If we choose  $h \leq h_0$ , where

$$h_0 = \left(\frac{\alpha_1}{8\tilde{k}}\right)^{1/2} \frac{1}{c_1 c_2 c_3},$$

then

$$\alpha_1 \|Q - Q_h\|_{1,\Omega} \leq 8c_1 \|Q - P_h\|_{1,\Omega}, \quad \forall P_h \in \mathbf{V}_h. \quad (\text{A } 12)$$

Next, substituting  $c_1$  from (A 7) and  $\tilde{k}$  from (A 8), the explicit form of  $h_0$  is

$$h_0 = \left(\frac{\alpha_1}{k + (a'/\eta^2) + (s''/\omega^2)}\right)^{1/2} \frac{1}{\sqrt{8}(c_0 + \beta'_1/\eta^2 + \beta'_2/\omega)c_2 c_3}.$$

Finally, using the interpolation theory result from the previous lemma, we see that the estimate (A 12) is bounded by a constant times  $h|Q|_{2,\Omega}$ , thus completing the proof. ■

## References

1. Hamley IW. 2003 Nanotechnology with soft materials. *Angew. Chem. Int. Ed.* **42**, 1692–1712. (doi:10.1002/anie.200200546)
2. Ozin G, Manners I, Fournier-Bidoz S, Arsenault A. 2005 Dream nanomachines. *Adv. Mater.* **17**, 3011–3018. (doi:10.1002/adma.200501767)
3. de-Gennes PG, Prost J. 1995 *The physics of liquid crystals*, vol. 83, 2nd edn. International Series of Monographs on Physics. Oxford UK: Oxford Science Publication.
4. Blinov L. 1983 *Electro-optical and magneto-optical properties of liquid crystals*. New York, NY: Wiley.
5. Goodby JW. 2012 Introduction to defect textures in liquid crystals. In *Handbook of Visual Display Technology* (eds J Chen, W Cranton, M Fihn), pp. 1290–1314. New York, NY: Springer.
6. Sun J *et al.* 2014 Preparation and thermo-optical characteristics of a smart polymer-stabilized liquid crystal thin film based on smectic A-chiral nematic phase transition. *Smart Mater. Struct.* **23**, 125038. (doi:10.1088/0964-1726/23/12/125038)
7. Hoogboom J, Elemans JA, Rowan AE, Rasing TH, Nolte RJ. 2007 The development of self-assembled liquid crystal display alignment layers. *Phil. Trans. R. Soc. A* **365**, 1553–1576. (doi:10.1098/rsta.2007.2031)
8. Dasgupta P, Das MK, Das B. 2015 Fast switching negative dielectric anisotropic multicomponent mixtures for vertically aligned liquid crystal displays. *Mater. Res. Express* **2**, 045015. (doi:10.1088/2053-1591/2/4/045015)
9. Mori H, Eugene CGJ, Kelly JR, Bos PJ. 1999 Multidimensional director modeling using the Q-tensor representation in a liquid crystal cell and its application to the  $\pi$ -cell with patterned electrodes. *Jpn J. Appl. Phys.* **38**, 135–146. (doi:10.1143/JJAP.38.135)
10. Mottram NJ, Newton CJP. 2014 Introduction to Q-tensor theory. *ArXiv e-prints*.
11. Tran L *et al.* 2017 Change in stripes for cholesteric shells via anchoring in moderation. *Phys. Rev. X* **7**, 041029 (doi:10.1103/PhysRevX.7.041029)
12. Lavrentovich MO, Tran L. 2020 Undulation instabilities in cholesteric liquid crystals induced by anchoring transitions. *Phys. Rev. Res.* **2**, 023128 (doi:10.1103/PhysRevResearch.2.023128)
13. Dogic Z, Fraden S. 2006 Ordered phases of filamentous viruses. *Curr. Opin. Colloid Interface Sci.* **11**, 47–55. (doi:10.1016/j.cocis.2005.10.004)
14. Oh DX, Cha YJ, Nguyen HL, Je HH, Jho YS, Hwang DS, Yoon DK. 2016 Chiral nematic self-assembly of minimally surface damaged chitin nanofibrils and its load bearing functions. *Sci. Rep.* **6**, 23245 (doi:10.1038/srep23245)

15. Agez G, Bayon C, Mitov M. 2017 Multiwavelength micromirrors in the cuticle of scarab beetle *Chrysina gloriosa*. *Acta Biomater.* **48**, 357–367. (doi:10.1016/j.actbio.2016.11.033)
16. Lagerwall JP, Scalia G. 2012 A new era for liquid crystal research: applications of liquid crystals in soft matter nano-, bio- and microtechnology. *Curr. Appl. Phys.* **12**, 1387–1412. (doi:10.1016/j.cap.2012.03.019)
17. Schwartz M, Lenzini G, Geng Y, Rønne PB, Ryan PYA, Lagerwall JPF. 2018 Cholesteric liquid crystal shells as enabling material for information-rich design and architecture. *Adv. Mater.* **30**, 1707382 (doi:10.1002/adma.201707382)
18. Martinez AM, McBride MK, White TJ, Bowman CN. 2020 Reconfigurable and spatially programmable chameleon skin-like material utilizing light responsive covalent adaptable cholesteric liquid crystal elastomers. *Adv. Funct. Mater.* **30**, 2003150 (doi:10.1002/adfm.202003150)
19. Geng Y, Kizhakhidathazhath R, Lagerwall JPF. 2022 Robust cholesteric liquid crystal elastomer fibres for mechanochromic textiles. *Nat. Mater.* **21**, 1441–1447. (doi:10.1038/s41563-022-01355-6)
20. Lagerwall J. 2023 Liquid crystal elastomer actuators and sensors: glimpses of the past, the present and perhaps the future. *Programmable Mater.* **1**, e9. (doi:10.1017/pma.2023.8)
21. Gartland Jr EC, Palffy-Muhoray P, Varga RS. 1991 Numerical minimization of the Landau-de Gennes free energy: defects in cylindrical capillaries. *Mol. Crystals Liquid Crystals* **199**, 429–452. (doi:10.1080/00268949108030952)
22. Bajc I, Hecht F, Žumer S. 2016 A mesh adaptivity scheme on the Landau–de Gennes functional minimization case in 3D, and its driving efficiency. *J. Comput. Phys.* **321**, 981–996. (doi:10.1016/j.jcp.2016.02.072)
23. Davis T, Gartland E. 1998 Finite element analysis of the Landau-de Gennes minimization problem for liquid crystals. *SIAM J. Numer. Anal.* **35**, 336–362. (doi:10.1137/S0036142996297448)
24. Bartels S, Raisch A. 2014 Simulation of Q-tensor fields with constant orientational order parameter in the theory of uniaxial nematic liquid crystals. In *Singular Phenomena and Scaling in Mathematical Models* (ed. M Griebel), pp. 383–412. Springer International Publishing.
25. Borthagaray JP, Nochetto RH, Walker SW. 2020 A structure-preserving FEM for the uniaxially constrained Q-tensor model of nematic liquid crystals. *Numerische Math.* **145**, 837–881. (doi:10.1007/s00211-020-01133-z)
26. Lee GD, Anderson J, Bos PJ. 2002 Fast Q-tensor method for modeling liquid crystal director configurations with defects. *Appl. Phys. Lett.* **81**, 3951–3953. (doi:10.1063/1.1523157)
27. Zhao J, Wang Q. 2016 Semi-discrete energy-stable schemes for a tensor-based hydrodynamic model of nematic liquid crystal flows. *J. Sci. Comput.* **68**, 1241–1266. (doi:10.1007/s10915-016-0177-x)
28. Zhao J, Yang X, Shen J, Wang Q. 2016 A decoupled energy stable scheme for a hydrodynamic phase-field model of mixtures of nematic liquid crystals and viscous fluids. *J. Comput. Phys.* **305**, 539–556. (doi:10.1016/j.jcp.2015.09.044)
29. Ravnik M, Žumer S. 2009 Landau-deGennes modelling of nematic liquid crystal colloids. *Liq. Cryst.* **36**, 1201–1214. (doi:10.1080/02678290903056095)
30. Čopar S, Ravnik M, Žumer S. 2014 Janus nematic colloids with designable valence. *Materials* **7**, 4272 (doi:10.3390/ma7064272)
31. Virga EG. 1994 *Variational theories for liquid crystals*, vol. 8, 1st edn. London, UK: Chapman and Hall.
32. Majumdar A. 2010 Equilibrium order parameters of nematic liquid crystals in the Landau-de Gennes theory. *Eur. J. Appl. Math.* **21**, 181–203. (doi:10.1017/S0956792509990210)
33. Sonnet AM, Virga E. 2012 *Dissipative ordered fluids: theories for liquid crystals*. New York, NY: Springer.
34. Barbero G, Durand G. 1986 On the validity of the Rapini-Papoular surface anchoring energy form in nematic liquid crystals. *J. Phys. France* **47**, 2129–2134. (doi:10.1051/jphys:0198600470120212900)
35. Fournier JB, Galatola P. 2005 Modeling planar degenerate wetting and anchoring in nematic liquid crystals. *Europhys. Lett. (EPL)* **72**, 403–409. (doi:10.1209/epl/i2005-10253-5)
36. Walker SW. 2018 On the correct thermo-dynamic potential for electro-static dielectric energy. (<http://arxiv.org/abs/1803.08136>)
37. Feynman RP, Leighton RB, Sands M. 1964 *The feynman lectures on physics*. Boston, MA: Addison-Wesley Publishing Company.

38. Biscari P, Cesana P. 2007 Ordering effects in electric splay Freedericksz transitions. *Contin. Mech. Thermodyn.* **19**, 285–298. (doi:10.1007/s00161-007-0055-8)
39. Eugene CGJ. 2018 Scalings and limits of Landau-de Gennes models for liquid crystals: a comment on some recent analytical papers. *Math. Modell. Anal.* **23**, 414–432. (doi:10.3846/mma.2018.025)
40. Hicks A. 2024 *Modeling and Numerical Analysis of the Cholesteric Landau–de Gennes Model*. LSU Doctoral Dissertations. (doi:10.31390/gradschool\_dissertations.6390)
41. Stynes M, Stynes D. 2018 *Convection diffusion problems: an introduction to their analysis and numerical solution*. Graduate Studies in Mathematics. AMS.
42. Maso GD, Forti M, Miranda M, Spagnolo SA, Ambrosio L (eds). 2006 *Selected papers*. Springer Collected Works in Mathematics. Ennio De Giorgi.
43. Wise SM, Wang C, Lowengrub JS. 2009 An energy-stable and convergent finite-difference scheme for the phase field crystal equation. *SIAM J. Numer. Anal.* **47**, 2269–2288. (doi:10.1137/080738143)
44. Xu J, Li Y, Wu S, Bousquet A. 2019 On the stability and accuracy of partially and fully implicit schemes for phase field modeling. *Comput. Methods Appl. Mech. Eng.* **345**, 826–853. (doi:10.1016/j.cma.2018.09.017)
45. Brenner SC, Scott LR. 2008 *The mathematical theory of finite element methods*, vol. 15, 3rd edn. Texts in Applied Mathematics. New York, NY: Springer.
46. Rathgeber F, Ham DA, Mitchell L, Lange M, Luporini F, Mcrae ATT, Bercea GT, Markall GR, Kelly PHJ. 2016 Firedrake: automating the finite element method by composing abstractions. *ACM Trans. Math. Softw.* **43**, 1–27. (doi:10.1145/2998441)
47. Balay S *et al.* 2016 PETSc Web page. See [www.mcs.anl.gov/petsc](http://www.mcs.anl.gov/petsc).
48. Demus D, Richter L. 1978 *Textures of liquid crystals*. Weinheim: Verlag Chemie.
49. Dierking I. 2003 *Textures of liquid crystals*. Darmstadt, Germany: Wiley–VCH Verlag GmbH & Co. KGaA.
50. Hicks A. 2024 andrewlhicks/q-tensor-3d: v0.1 (v0.1). Zenodo. (doi:10.5281/zenodo.10929107)
51. Hicks A. 2024 andrewlhicks/sympyplus: v0.1 (v0.1). Zenodo. (doi:10.5281/zenodo.10929109)
52. Hicks A. 2024 andrewlhicks/mymesh: v0.1 (v0.1). Zenodo. (doi:10.5281/zenodo.10929113)
53. Giaquinta M, Martinazzi L. 2012 *An introduction to the regularity theory for elliptic systems, harmonic maps and minimal graphs*. Publications of the Scuola Normale Superiore. New York, NY: Springer.